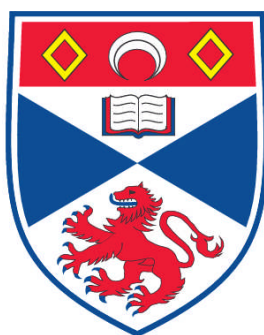


**MICROLENSING FOR EXTRASOLAR PLANETS:
IMPROVING THE PHOTOMETRY**

David J. Bajek

**A Thesis Submitted for the Degree of MPhil
at the
University of St. Andrews**



2012

**Full metadata for this item is available in
Research@StAndrews:FullText
at:**

<http://research-repository.st-andrews.ac.uk/>

Please use this identifier to cite or link to this item:

<http://hdl.handle.net/10023/3372>

This item is protected by original copyright

**This item is licensed under a
Creative Commons License**

DAVID J. BAJEK
University of St Andrews
Physics and Astronomy
Submitted September 2012

Microlensing for Extrasolar Planets: Improving the Photometry

MPhil

Supervisor: Professor Keith Horne

Gravitational Microlensing, as a technique for detecting Extrasolar Planets, is recognised for its potential in discovering small-mass planets similar to Earth, at a distance of a few Astronomical Units from their host stars. However, analysing the data from microlensing events (which statistically rarely reveal planets) is complex and requires continued and intensive use of various networks of telescopes working together in order to observe the phenomenon. As such the techniques are constantly being developed and refined; this project outlines some steps of the careful analysis required to model an event and ensure the best quality data is used in the fitting. A quantitative investigation into increasing the quality of the original photometric data available from any microlensing event demonstrates that 'lucky imaging' can lead to a marked improvement in the signal to noise ratio of images over standard imaging techniques, which could result in more accurate models and thus the calculation of more accurate planetary parameters. In addition, a simulation illustrating the effects of atmospheric turbulence on exposures was created, and expanded upon to give an approximation of the lucky imaging technique. This further demonstrated the advantages of lucky images which are shown to potentially approach the quality of those expected from diffraction limited photometry. The simulation may be further developed for potential future use as a 'theoretical lucky imager' in our research group, capable of producing and analysing synthetic exposures through customisable conditions.

1. Candidate's declarations:

I, David Bajek, hereby certify that this thesis, which is approximately 17,500 words in length, has been written by me, that it is the record of work carried out by me and that it has not been submitted in any previous application for a higher degree.

I was admitted as a research student in September 2011, and as a candidate for the degree of MPhil in September 2012; the higher study for which this is a record was carried out in the University of St Andrews between 2011 and 2012.

Date 22 Sep 2012
Signature of candidate

2. Supervisor's declaration:

I hereby certify that the candidate has fulfilled the conditions of the Resolution and Regulations appropriate for the degree of MPhil in the University of St Andrews and that the candidate is qualified to submit this thesis in application for that degree.

Date 22 Sep 2012
Signature of supervisor

3. Permission for electronic publication: (to be signed by both candidate and supervisor)

In submitting this thesis to the University of St Andrews I understand that I am giving permission for it to be made available for use in accordance with the regulations of the University Library for the time being in force, subject to any copyright vested in the work not being affected thereby. I also understand that the title and the abstract will be published, and that a copy of the work may be made and supplied to any bona fide library or research worker, that my thesis will be electronically accessible for personal or research use unless exempt by award of an embargo as requested below, and that the library has the right to migrate my thesis into new electronic forms as required to ensure continued access to the thesis. I have obtained any third-party copyright permissions that may be required in order to allow such access and migration, or have requested the appropriate embargo below.

The following is an agreed request by candidate and supervisor regarding the electronic publication of this thesis:

(i) Access to printed copy and electronic publication of thesis through the University of St Andrews.

Date 22 Sep 2012
Signature of candidate

Signature of supervisor

Foreword & Acknowledgements

Since beginning my astronomy project in Extrasolar Planets detected by Gravitational Microlensing at St Andrews University, I have developed many essential and transferable skills, as well as gained immense and invaluable knowledge in a wide and fascinating field. In particular I have succeeded in Professor Keith Horne's Astronomical Data Analysis course, a SUPA Advanced Data Analysis course, and a Statistics Workshop, all of which have greatly developed my understanding of statistics, computing and modelling in several coding languages. I have also taken part in the group's annual RoboNet microlensing workshop in Pasadena, California, which introduced me to members of the global team and their individual roles in the group. I have since attended several conferences, including "Science with a Wide-Field Infrared Telescope in Space", and "The 16th International Conference on Gravitational Microlensing", which have furthered my communal contacts in the field, reinforced my understanding of the subject and provided great insight into its future, some of which is discussed herein. On top of some collaborative publications, I am also pleased to have been invited to work directly with my supervisor in a paper which is currently in development, "Photometric Potential of Lucky Imaging", some of which is outlined within this thesis.

As well as acknowledging the STFC for the scholarship which made this project possible, I also wish to sincerely thank both Professor Keith Horne and Dr Markus Hundertmark for their constant support and encouragement since joining the research group.

Table of Contents

LITERATURE REVIEW

1.0 Extrasolar Planets	4
- 1.1 'Exoplanets', An Introduction	4
- 1.2 Detection Methods	5
2.0 Gravitational Microlensing Overview	7
- 2.1 History	7
- 2.2 Potential	7
- 2.3 Theoretical Summary	10
- 2.4 Recent Developments & Further Potential	15
2.4.1 Mesolensing	15
2.4.2 Unbound Planets	17
2.4.3 A Cosmic Double-Slit Experiment	20

RESEARCH

3.0 Microlensing: Fitting, Improving & Simulating	21
- 3.1 Fitting Microlensing Data	21
3.1.1 Raw Data, Errors and Suitable Models	21
- 3.2 Optimising the Data Selection	26
3.2.1 The Reductions Pipeline	26
3.2.2 Further & Future Improvements	29
- 3.3 Microlensing Photometry: Improvements from Theory	30
3.3.1 Lucky Imaging Sound to Noise Ratio	30
3.3.2 Considering a Moffat PSF	43
3.3.3 Simulating Seeing-Limited Exposures	49
3.3.4 Limitations & Future Expansion of the Simulation	63
4.0 Conclusions	64
5.0 Future Work	65
- 5.1 Constraints on Microlensed Systems using Lucky Imaging	65
- 5.2 Observing	65
6.0 Publications	66
7.0 References	67

1.0 Extrasolar Planets

1.1 'Exoplanets', An Introduction

Though speculated upon for millennia and hypothesised for centuries, the existence of extra solar planets was not confirmed until the latter part of the 20th century, when in 1992 Wolszczan and Frail^[1] (using what would come to be recognised as the 'Pulsar Timing Method') discovered 'PSR B1257+12B'; a planet orbiting a pulsar star 980 lightyears away and widely considered to be the first definitively confirmed extrasolar planet. Since then, the number of extrasolar planets discovered has risen exponentially each year, with over 760 'exoplanets' confirmed as of 2012^[2], see Figure 1.

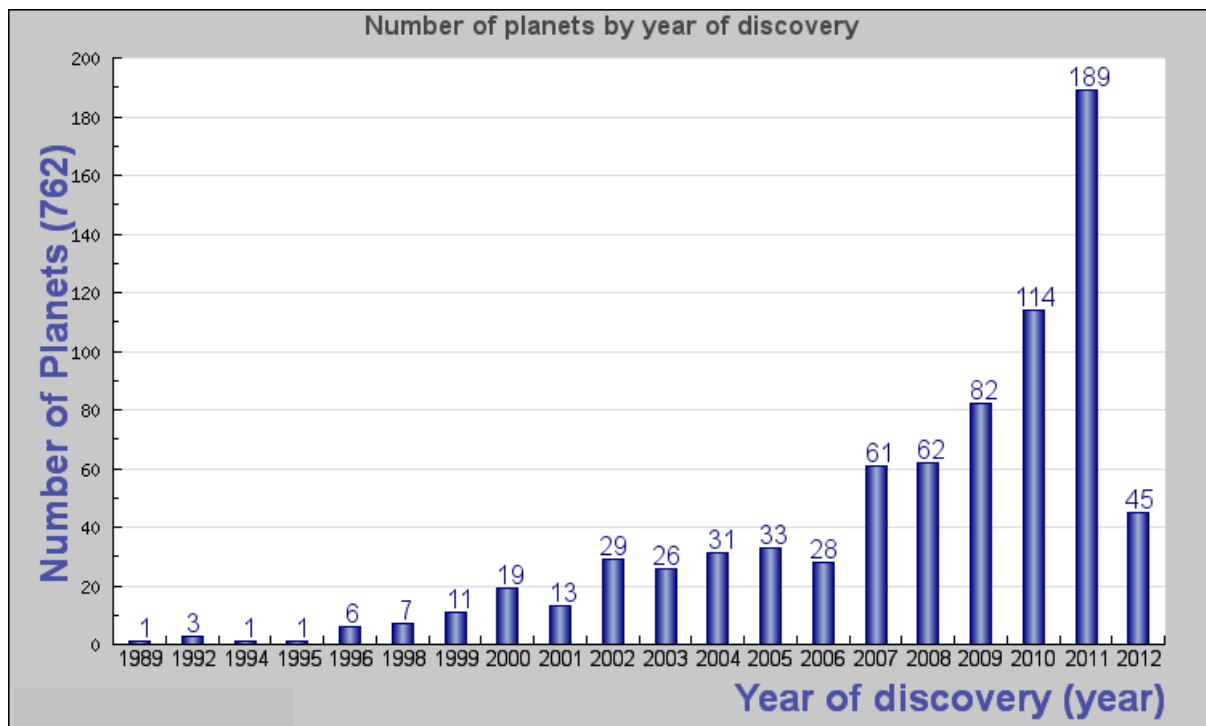


Figure 1 - The number of extra solar planets discovered each year has increased rapidly as new methods are developed and observing and survey techniques are finessed. Note that the '1989' entry predates the Wolszczan and Frail definitive 'first discovery' of 1992, as the candidate was not officially verified until several years later. Custom-Generated from the Extrasolar Planets Encyclopedia^[2]

Note: *The Extrasolar Planets Encyclopedia*^[2] is an important resource which works closely with many collaborating research groups in their respective fields in order to make available to the public the details of confirmed extrasolar planets and their host stars.

By searching for and analysing trends in discovered exoplanets based on their astronomical environments, and categorising their characteristics, we learn more about the formation, present state and future of Earth and our own solar system, and can over time rely less on hypotheses and theory and instead make direct correlations.

We then begin to understand the astronomical environments which are potentially capable of developing life (at least, 'as we know it'), and in turn begin to estimate the abundance of habitable planets, and perhaps even the likelihood of any which may already be inhabited.

In essence, to study extrasolar planets is to gain insight into what we already understand to be true about our solar system, to reduce misnomers and determine whether we as a 'living planet' are either an extremely rare case of random coincidences in the Universe, or are indeed merely a footnote in a plethora of abundant and diverse Universal life.

1.2 Detection Methods

As well as gravitational microlensing, several extra solar planet detection methods have been developed and improved since the first detection, each adopted to suit a particular investigatory niche or constrain a specific star or planetary parameter, whereby there is a need for various research groups to collaborate in order to confirm their findings by the use of one or several combinations of these methods^[3]:

Pulsar timing:^[1] Pulsar stars 'pulse' in radio waves at regular intervals with variations on the order of around 10^{-12} seconds per year, and thus when a planet is in orbit, it causes a detectable discrepancy in the timing of these pulses. For a planet of mass M_p in a circular orbit with semi-major axis a_p and inclination i around a star of mass M_* , the maximum amplitude of the delay time may be given by

$$\tau = \sin i \left(\frac{a_p}{c} \right) \left(\frac{M_p}{M_*} \right)$$

The immense sensitivity of this method allows for the detection of very low mass planets, however the relative rarity of pulsar stars makes finding many extrasolar planets by this method fairly difficult. As such, by extension the method may be adopted to suit studies involving eclipsing binaries, or indeed for investigating single star systems, as their intrinsic pulsations may also be timed.

Imaging:^[4] Though observing extrasolar planets by imaging them directly does occur, the method is difficult due to the extremely low light output from distant planets as compared to their bright host stars, whose glare can effectively saturate over the contribution from the planet. The important factor is the ratio of brightness (luminosity L) between the host star and the planet of radius R_p and semi-major axis a_p given for a planetary atmosphere which is the product of the geometric albedo A and the particle phase function $p(\varphi(t))$:

$$L_p/L_* = Ap(\varphi(t)) \left(\frac{R_p}{a_p}\right)^2$$

As such, those exoplanets discovered by direct imaging tend to be both very large and at wide separations from their host stars. However, the brightness saturation issue may be overcome by the use of specialised coronagraphs, which may be adapted to effectively block the light from the source. In 2004, '2M1207b' was the first extrasolar planet discovered using this method^[50].

Gravitational Microlensing: The phenomenon whereby light from a distant background star is deviated and magnified by the gravitational influences of a foreground star. If a planet is present in the star system, there is a chance that its own gravitational field will also lead to an additional detectable magnification in the resulting lightcurve; *see section 2.0*

Radial Velocity:^[5] A system with a planet and its host star have a common centre of mass, about which they both orbit. Discrepancies in the star's radial velocity may be detected due to the Doppler Effect as a result of perturbations in the star's spectral lines. This method is applicable to a wide variety of stars and thus to date has proved the most productive method. The radial velocity method however is not capable of finding a planet's actual mass, but may simply place a lower limit on the mass. This can in some cases be overcome by using this method in combination with the 'transiting method'.

Transiting:^[6] An effect which occurs when a planet travels directly in front of its host star's disk, both in line with the observer, causing the measured brightness of the star to drop proportionally, depending on the relative area of the planet as compared to the star. As such this method is particularly capable of determining the extrasolar planet's radius. A disadvantage of this method is the requirement for *observer-planet-star* alignment, and thus the greatest probability for detection is for planets with small orbital separations (and preferably of relatively large radius); that is to say this method is best suited to finding candidates such as 'hot Jupiters'.

Astrometry:^[7] This technique involves the precise measurement of a star's position followed by observing the position change over time, where it is possible to observe the motion of such a star due to the gravitation of a planet orbiting it. Such a small motion is very difficult to measure, and so aside from a number of disputed detections, the method has not been very fruitful. However, it is still a highly important procedure to develop, as it has great potential in following up confirmed planets and examining their properties where the detection method is not capable of doing so. The Global Astrometric Interferometer for Astrophysics (GAIA) space mission^[8] (due to be launched in 2013) will be utilising astrometric techniques to catalogue over 1 billion stars.

2.0 Gravitational Microlensing Overview

2.1 History

The phenomenon which occurs in relativity when the gravitational field of a massive object such as a star (the 'lens'), acts in principle like that of the stem of a wine glass; magnifying the light of a distant star (the 'source') behind it. As the lens star approaches and crosses the source star, the gravitation causes the light from the source star to be redirected and bend around the lens star towards the observer (in the case of perfect observer-lens-source alignment, this gives rise to the source image appearing as an Einstein Ring encircling the lens in the centre), leading to a characteristic *light magnification curve*. If a planet is orbiting the lens star, this can cause detectable perturbations in the curve. Though comparatively few planets have been discovered using this method, it is sensitive to planets up to fairly wide separations from their host stars, and particularly for planets close to the Einstein Radius (the radius of an Einstein Ring), and varying over a wide range of planetary masses.

The original basis of the phenomenon is buried in historical legacy, from Isaac Newton's suggestion as early as 1704 that gravity may be able to bend light rays, to the highly important introduction of relativity to the concept in 1936, when Albert Einstein published his calculations on the "Lens-Like Action of a Star by the Deviation of Light in the Gravitational Field"^[9]. Einstein described this is a "most curious effect", though ironically remarked in the paper that "there is no great chance of observing this phenomenon". This remark was finally to be proven wrong in 1993, when the first microlensing event was detected and reported on by C. Alcock and the MACHO collaboration (Massive Astrophysical Compact Halo Object) in their publication "Possible Gravitational Microlensing of a Star in the Large Magellanic Cloud"^[10]. Finally, in 2004 the first extrasolar planet to be detected by gravitational microlensing, 'OGLE-2003-BLG-235Lb / MOA-2003-BLG-53Lb', was discovered by *Bond et al*^[57] and characterised as a 1.5 Jupiter-Mass Gas Giant.

2.2 Potential

Gravitational Microlensing is one of the few detection methods that is capable of finding cold, rocky planets around very distant stars. Unlike transit or radial velocity methods, microlensing has the benefit of being fairly sensitive to planetary candidates near the habitable zone. Along with radial velocimetry, it is also one of few methods which could realistically detect Earth-mass planets from the ground. Unlike, for example the transit method, microlensing is not confined or limited just towards finding large Jupiter-like planets at small semi-major axes, and therefore could give rise to a far fairer overall census of extrasolar planetary systems. The microlensing effect also has the added benefit of being wavelength-independent, as it relies only on the relative magnification of the signal, thus allowing the study of objects radiating in any wavelength. It has come under the spotlight in recent years and is of particular interest as it is also capable of detecting 'free floating' or 'rogue' planets, particularly in conjunction with direct imaging surveys.

The major disadvantage however, is that specific systems cannot be selected for study due to the one-time nature of any microlensing event (any given event will not occur again, unlike the calculable and repeated nature of a transiting event), and in addition the probability of alignment between earth and any given lens and source stars is very low and unpredictable. And so instead microlensing events involve targets of opportunity and must be viewed by several observers at the same time for maximum collaboration on the results, and thus the issue is overcome by large survey teams (such as MOA and OGLE) constantly looking at large starfields and reporting on opportune magnifications to follow up teams, who may then model the light curves and collaborate to determine possible planetary candidates which may be examined further. Since the duration of events is typically from hours to days, it is necessary to have coordinated observations from many observatories around the globe in order to overcome the Earth rotating one telescope's view away from the target.

Finally, given that the candidate planet's star is so distant, detailed studies of the host are very difficult, and thus gaining precise orbital parameters of the planet is only possible for a select few events, and in addition the resultant light curves are complex and require in-depth analysis. As such, to date only 15 out of the hundreds of confirmed extra solar planets have been discovered by the microlensing method (April 17th 2012), and are summarised below in order of increasing Jovian mass, *see figure 2^[2]*.

Planet Name	Planet Mass M_j	Semi-Major Axis AU	Star Distance pc	Star Mass M_\odot
MOA-2007-BLG-192-L b	0.01	0.66	700	0.06
OGLE-2005-BLG-390L b	0.017	2.1	6500	0.22
MOA-2009-BLG-266L b	0.0327	3.2	3040	0.56
OGLE-2005-BLG-169L b	0.04	2.8	2700	0.49
OGLE-2007-BLG-368L b	0.0694	3.3	5900	0.64
MOA-2009-BLG-319 b	0.157	2	6100	0.38
MOA-2008-BLG-310-L b	0.23	1.25	6000	0.67
OGLE2-2006-BLG-109L c	0.271	4.5	1510	0.51
OGLE-2006-BLG-109L b	0.727	2.3	1510	0.51
MOA-2007-BLG-400-L b	0.9	0.85	6000	0.35
MOA-2011-BLG-293L b	2.4	1	7150	0.44
MOA-2009-BLG-387L b	2.6	1.8	5700	0.19
OGLE235-MOA53 b	2.6	5.1	5200	0.63
OGLE-2005-BLG-071L b	3.5	3.6	3300	0.46
MOA-bin-1 b	3.7	8.3	5100	0.75

Figure 2^[2] - A summary of the planets in the interactive extrasolar planet catalogue whose discoveries are attributed to gravitational microlensing, ordered by increasing Jovian Mass. Note the naming convention for planets tends to include which survey team was responsible (e.g. MOA, OGLE), the year of discovery, the location (e.g. the galactic bulge, BLG), and the event number and system specifics.

Note that for 'microlensed' planets, a large proportion of which are both low mass and at wide separations from their host stars which are located at large distances from Earth, may be contrasted with those discovered by, for example, the planets discovered by the transiting method.

The contribution of planets discovered by gravitational microlensing to the overall catalogue of all discovery methods can be seen in a compiled extrasolar planet summary diagram, see *figure 3*. The planets are plotted firstly for each detection method, and then for the parameters of Planet Mass, Orbital Radius and Orbital Period, where our local solar planets (yellow initials) mark comparable references, with Earth (E) at the centre for normalisation.

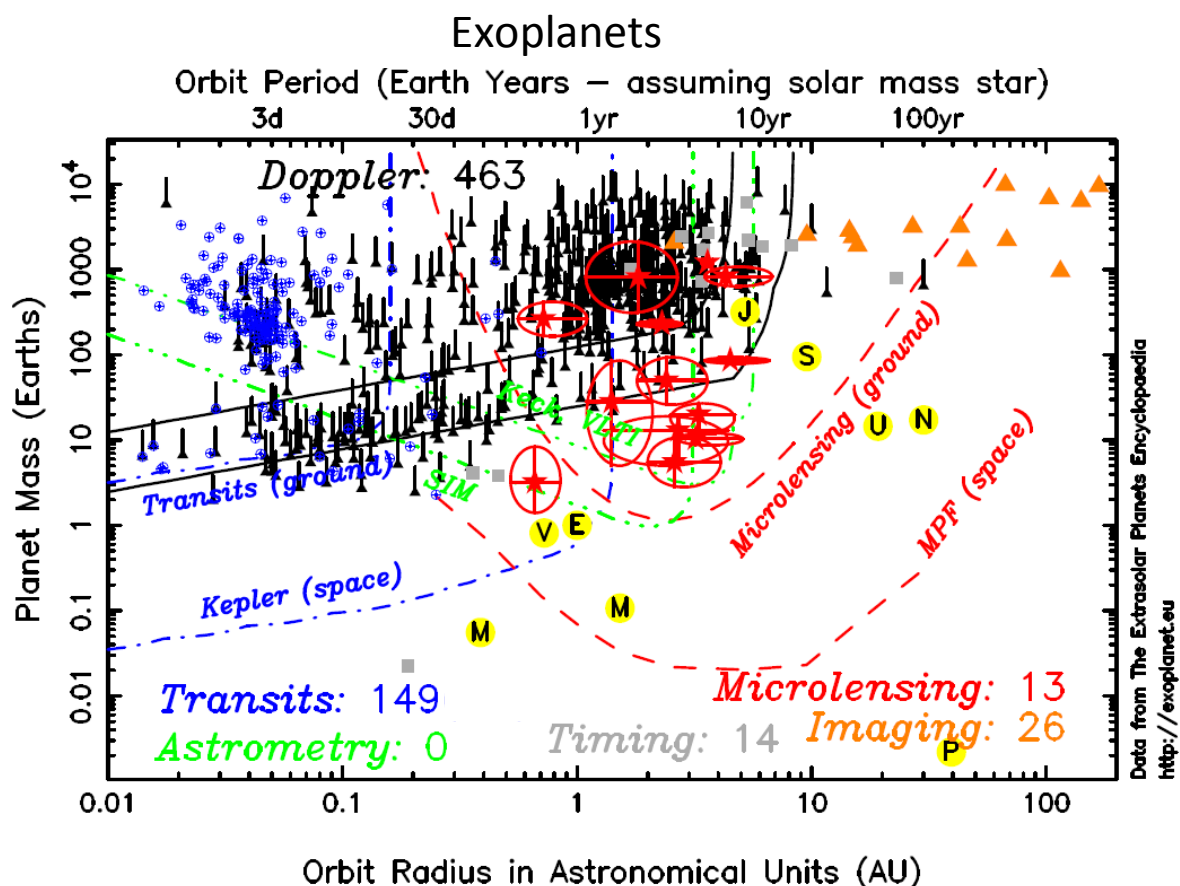


Figure 3 - A summary of all extrasolar planets discovered as of this year (data taken from The Extrasolar Planets Encyclopaedia), where Earth is a central reference point and the detection methods are highlighted by colour. The zones (i.e. parameters) down to which each method is potentially sensitive are illustrated by the highlighted region (lines) in their respective colour.

The parameters down to which each detection method is potentially sensitive are also highlighted, and reveal the niche of each type. As can be seen, the vast majority of the planets which have been discovered to date are located in the upper left quadrant of the diagram with respect to Earth, which is not surprising given that most of the method's sensitivities are confined to around this region; for example as discussed in *section 1.2*, the transiting method is most sensitive to large mass (i.e. large radius) planets, which are at low orbital separations from their host stars, and ideally with short orbital periods (i.e. the disk

of the planet is large in the plane of the host star, leading to a maximum dip in the light curve). Another method whose unique sensitivity is well illustrated is that of the direct imaging method; the discovered planets tend to be found in the upper right quadrant of the diagram, which exemplifies the need for planets to be of high mass (i.e. large radius) and at wide separations from their host star in order to maximise the detected light output from it as compared with the significantly brighter output of its host star.

However, looking at the sensitivity region of microlensing^{[51],[52]} which (from ground-based operations) extends into larger orbital radii and smaller masses in the lower right quadrant of the diagram, it is clear to see the potential and unique niche of this detection method. Further highlighted is the significant improvement which may be gained from microlensing in space-based operations, where observations are diffraction limited. This serves to accentuate the importance of imaging without the problems which arise as a result of atmospheric seeing (such as the photometric improvements of lucky imaging, *see section 3.3.1*), and further illustrates that whilst gravitational microlensing is perhaps not as fruitful as other detection methods, its sensitivity to otherwise undetectable parameters makes it an essential phenomenon to develop upon. WFIRST^[11] (Wide-Field Infrared Survey Telescope) is a proposed space observatory due for launch in 2020, one of whose missions is a space-based gravitational microlensing search for extrasolar planets.

2.3 Theoretical Summary

One of the most crucial and intensive aspects of Gravitational Microlensing is modelling the event based on observations in order to ascertain whether or not the system is host to a planet, and then constrain its parameters. As such many research groups dedicate time and resources utilising and designing complex software to fit the models and compare the results with collaborators for best results. The basic mathematics of the general light curve are outlined here (similarly as is described both by Gould^[12] and Horne^[13]), and used subsequently in the modelling aspects, *see section 3.1.1*

The light curve is fit to an event's data points by making the assumptions that the source star is a point, and that the lens star is a single point mass moving linearly, that is to say the 'point source-point lens approximation' (PSPL). The bend or deflection angle α formula of the light path may be given in terms of the Schwarzschild Radius S_L of the lens star with mass M_L and impact parameter r given the gravitational constant G :

$$S_L = \frac{2GM_L}{c^2} \quad (1)$$

and

$$\alpha = \frac{2S_L}{r} = \frac{4GM_L}{c^2 r}. \quad (2)$$

The nature of the light ray being deflected from the background star by the gravitational field of the lens star may be conveyed analogously with the standard lens equation; a 'focal length' f with respect to an observer, where d_s is now the distance from an observer (i.e. at Earth) to the source star, and d_L is the distance from an observer to the lens star in between;

$$\frac{1}{f} = \frac{1}{d_s - d_L} + \frac{1}{d_L} . \quad (3)$$

See *figure 4* for a representation of the relative positions of the observer, source star and lens star for a microlensing event in this regime.

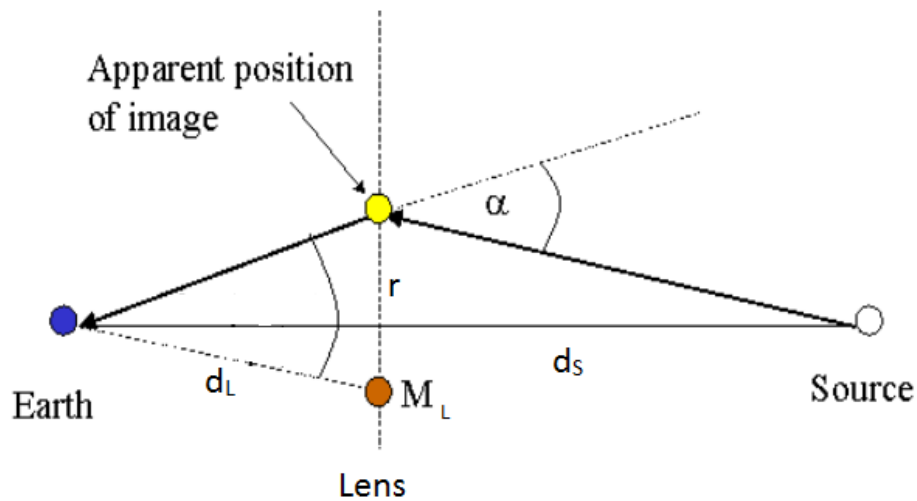


Figure 4 - An illustration of light from a source star bending around a lens star due to gravitational microlensing, resulting in the source star's image being viewed from Earth at some deviated position which will depend on the overall alignment.

It follows trigonometrically that the radius of the Einstein Ring r_E may be determined from the bend angle, such that

$$f = \frac{r_E}{\alpha} = \frac{r_E^2 c^2}{4GM_L} , \quad (4)$$

and thus

$$r_E = \sqrt{\frac{4GM_L}{c^2} \frac{d_L(d_s - d_L)}{d_s}} , \quad (5)$$

Where the Einstein radius may be represented alternatively as the *angular* radius ϑ_E of the Einstein ring; in the event of perfect alignment between the source and lens stars

$$\theta_E = \frac{r_E}{d_L} = \sqrt{\frac{4GM_L}{c^2} \frac{d_S - d_L}{d_S d_L}} \quad (6)$$

For illustrative purposes it is worth noting that for a lens star of mass approximately equal to the mass of the Sun, a typical Galactic Bulge microlensing event has $d_L = 5$ kpc, and $d_S = 10$ kpc, giving R_E on the order of 4 AU, corresponding to ϑ_E on the order of 0.8 milliarcseconds^[13].

The magnification factor A is the relative proportion by which the brightness measured from the source star is increased, and depends on the closeness of the alignment of the observer, the lens star and the source star

$$A(u) = \frac{u^2 + 2}{u\sqrt{u^2 + 4}} \quad (7)$$

Where u is the separation between the lens and source stars, conveniently in units of the angular Einstein Radius. The magnification increases as u decreases, such that when the source/lens separation u approaches 0, the images converge on an Einstein Ring. Conversely, at particularly wide separations, as expected there is no detectable magnification. However, in the typical intermediate separation case which is observed, two images (major and minor) of the source star are produced at positions which vary over time with the varying alignment (i.e. the relative motion of the two stars during the event), see *figure 5*.

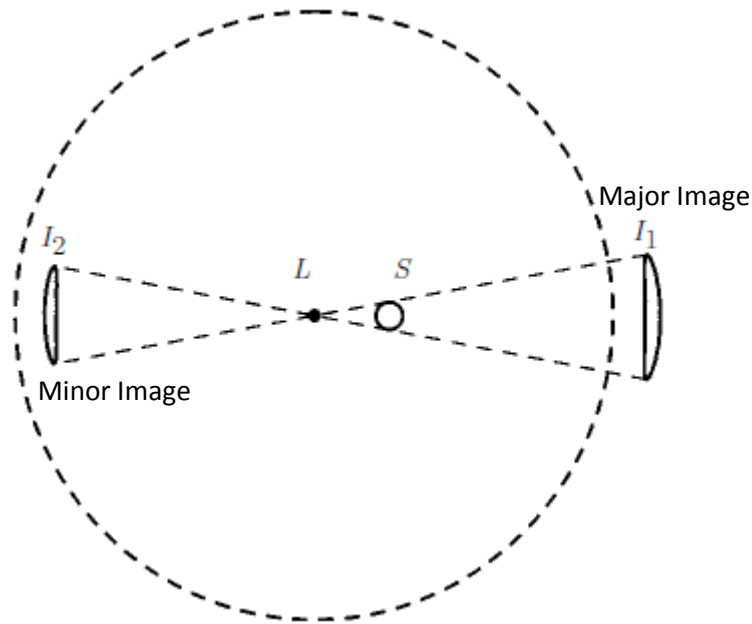


Figure 5 - A diagram of how a microlensing event may appear to an observer as compared with looking down the stem of a wine glass, where the gravitational field of the lens star L causes light from the source star S to be magnified and redirected. In the case of near alignment, two images I_1 and I_2 of the source star are formed; a major image outside and a minor image within the theoretical Einstein Ring. Note, the actual position of the source star is not technically seen, only the resultant images. Image adapted from Paczyński et al, 1996^[14].

The most relevant time scale during the event is the Einstein time t_E , and is the relative time needed for the lens star to traverse an angular distance ϑ_E relative to the source star. The function $u(t)$ may be acquired by simple use of Pythagoras, where

$$u(t) = \sqrt{u_{min}^2 + \left(\frac{t-t_0}{t_E}\right)^2} \quad (8)$$

The minimum separation between the source and lens stars is u_{min} , and as per the magnification light curve described by Paczyński et al, 1996^[14], determines the peak (maximum) brightness of the event, defined as occurring at time t_0 , see figure 6.

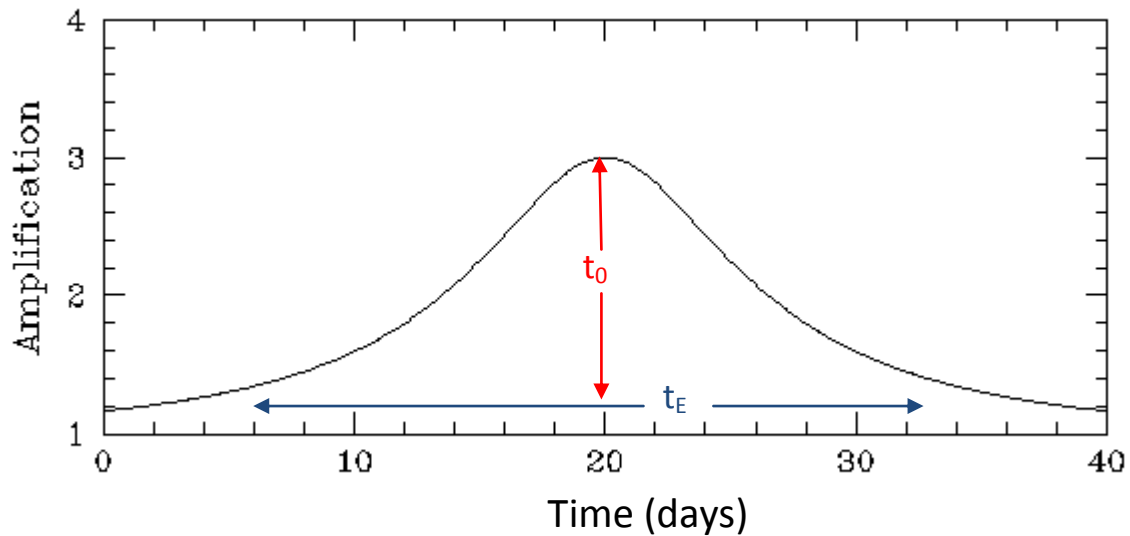


Figure 6 - A typical light magnification curve from a microlensing event, where the peak magnification occurs at time t_0 (the closest alignment between the observer, source star and lens star) and the overall event is seen to occur over the duration of the Einstein Time t_E . Note, the magnification is relative to a baseline 'unmagnified' level, and is thus normalised to a magnification of 1.

If during the alignment a planet is present in the system, its mass too will cause a detectable magnification in the light curve, distinctive from that caused between the two stars, and appears as an additional artefact, *see figure 7*. The shape of this artefact will depend greatly on the planet's characteristics (such as mass and semi-major axis), but also on the relative position of the planet on the course of the alignment.

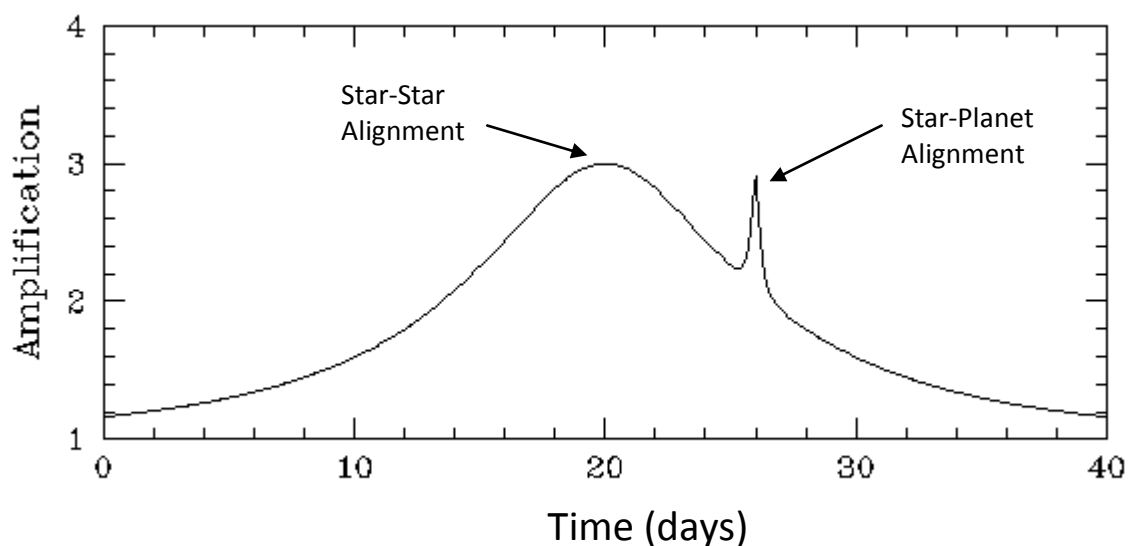


Figure 7 - An additional peak in the regular light curve of a microlensing event is caused by the mass of a planet in the system magnifying the light from the source star for a second time, and may be analysed to determine the characteristics of the planet.

Careful mathematical modelling and computer simulations of the event will reveal these planetary characteristics (or indeed whether the event represents some type of binary star system rather than a planet) and is one of the most complex and labour-intensive aspects of the Gravitational Microlensing hunt for extrasolar planets.

2.4 Recent Developments & Further Potential

As with any branch of science, Gravitational Microlensing is constantly being developed and the methodologies improved and expanded upon for use in various avenues of research. It is widely recognised as an important scientific tool with massive potential, of which some of the most recent breakthroughs are outlined herein.

2.4.1 Mesolensing

A relatively recently considered phenomenon in the field of microlensing which is attracting great interest is *mesolensing*; essentially, microlensing by lens stars which are very close to our own solar system, rather than distant stars towards the Galactic Bulge.

The need for the lens and source stars to be in alignment with earth in microlensing events renders the occurrence to be very rare, to the extent that for alignment with an observer on Earth, fewer than one in a million stars in the Galactic Bulge are expected to be microlensed at any given time (that is to say, at least one million stars would have to be carefully observed in order to detect a microlensing event).

As well as the rarity of alignments between a lens and source star separated by massive distances (for typical microlensing events many thousands of lightyears), the majority of them occur between stars which are both also very distant from us (often over halfway between earth and the galactic centre). At these enormous distances, the possibility is lost of immediately measuring with ease the motion of the lens star relative to others (until, depending on the relative velocity, several years later), and so there is no way to accurately predict when any lens and any source star will be aligned; problems which may be overcome by so-called mesolensing. The effect has been extensively investigated by *R. Di Stefano*, some of whose work and collaborations are outlined herein.

The 2005 publication "Mesolensing Explorations of Nearby Masses: From Planets to Black Holes"^[15] explores the many cosmological applications and the overall potential of mesolensing, including the study of forms of matter which remain 'undiscovered', from intermediate-mass black holes, to galactic dark matter. The implications were further examined in 2009^[16], including the potential of mesolensing to determine realistic limits on the proportion of dark matter which consists of MACHOs, as well as investigating the population of binary systems in galaxies.

In terms of extra solar planets, *Di Stefano* highlights that mesolensing is especially sensitive to finding those with an orbital distance equal to that of the Einstein radius, which itself is typically particularly close to that of the habitable zone (that is, the zone around a star in which the stellar circumstances could maintain liquid water on a planet, and thus may be capable of sustaining Earth-like life). The mesolensing Angular Einstein Radius and proper motions tend to be larger than typical for microlenses^[17], producing a larger probability that a system nearby our own will serve as a lens, thus widening the potential for new modes of observational study. The higher predictability of the relative positions and likelihood of a lensing event also leads to the ability to calculate the proper motion using astrometry; the larger lensing angle of mesolensing could lead to a directly measurable shift in the observed apparent brightness of the source star, and in its position.

If there happen to be planets orbiting the star, the greater lensing angle also offers the ability to study the effect of planets with low orbital separations; thus if one can extrapolate the trajectory of a nearby star, then mesolensing can be predicted in advance based on the proximity of background sources along the path, leading to the development of a new type of *mesolensing survey*.

Di Stefano outlines that mesolensing would in fact have "all the potential for detecting exoplanets" as in conventional microlensing, "with the added bonus that the lens system would be much more amenable to follow-up observations"^[18]. This is particularly of interest given that for ideal circumstances, the planet could conceivably be confirmed with additional detection methods, and more information on such a planet and its host-star may be gained, as well as focussed (and prioritised) selection for those which are lensing in the habitable zone.

More recently, in 2012 *Di Stefano* investigated a particular case, object VB 10^[19]; a low-mass star less than 20 lightyears away, with a rapid (but measurable) angular shift per year. Previously, HST images had revealed a faint object in its mapped path, a distant background star which is both dimmer and bluer than the lens, and was predicted to arrive in the lensing zone of VB 10 in early 2012. Though the potential is exciting, the mesolensing by VB 10 is not entirely an ideal case, given that such a close star moving so quickly with a high relative brightness does not provide the best suited set of experimental conditions.

Di Stefano's investigation involved the study of the lensing signatures associated with hypothetical planets orbiting nearby high proper-motion stars at widely varied separations to provide a guide for observers on this event, as well as future predicted ones. In the case of VB 10 they determine that an observing plan which involved targeting the star several times per night at each of several longitudes will either detect planets, or else at least place weak limits on possible parameters.

The continued work of *Lépine and Di Stefano* in 2012^[18] regarding VB 10 most recently estimated a 50% probability that the closest approach between the lens and host stars will be less than 100 milliarcseconds, a 20% probability of less than 50 milliarcseconds, and a 10% probability of a separation of less than 20 milliarcseconds. At 20 milliarcseconds of separation they calculate the resultant microlensing effect would give rise to an increased relative magnification from the source star of 6%, and corresponding with a 3.3 milliarcsecond astrometric shift. They note that the best possibility of observing such an event would be in the blue optical band, given this is the lowest brightness ratio between the lens and source stars.

The exciting indication is that if their star is indeed host to a Jupiter-mass planet at a semi-major axis approximately between 0.18 and 0.84 astronomical units, there is a reasonable probability that this will result in a higher magnification secondary event, that is to say the first *mesolensing event* to reveal a planet.

2.4.2 Unbound Planets

The existence of unbound or rogue planets (defined as free-floating objects of planetary mass by IAU^[53]), a low-mass object which is not gravitationally bound to any host star^[20], is neither historically unanticipated, nor scientifically unexpected; they have been predicted from simulated models of solar-system formation, where the process is the same as for bound planets but they are scattered from the system by gravitational interactions between each other. Planet-formation theory suggests that systems with multiple giant planets (such as Jupiter) could scatter smaller planets into particularly wide separations, and potentially far enough to even become entirely unbound from the host star and allowed to orbit the galaxy directly.

Some of the greatest work and most promising future studies in this area have come about from gravitational microlensing. In 2011, *Takahiro Sumi et al* from the MOA and OGLE collaborations published a study which they had carried out of past microlensing events^[21]. They observed 50 million stars using the 1.8m telescope located at Mount John Observatory, along with the 1.3m Warsaw University Telescope which is based at Las Campanas Observatory. Out of 474 confirmed microlensing events, 10 were reported to have lasted for very short durations (less than 48 hours, suggesting very low mass objects), 7 of which were later definitively confirmed by data from their OGLE counterpart collaborators.

The candidates are estimated to be unbound planets of approximately Jovian-mass, with no stars having been observed within 10 astronomical units of the event. Such unbound planets are estimated by Sumi to be in the region of two times as frequent as main-sequence stars.

The distinction is made between these candidates and, for example, stars and brown dwarfs due to the abrupt change (at Jupiter mass) in the mass function in their measurements. The possibility is still recognised that these planets may perhaps have a host star at very wide separations, however direct imaging of extrasolar planets by other teams suggests that such widely separated planets are very rare.

However, the implied rarity of planets at wide orbital separations of their stars, and thus the calculation of the abundance of free-floating unbound planets, was recently contested in part by *Quanz et al* in 2012^[22], who's team investigated the constraints which the direct imaging detection method may place on the estimated abundance of unbound planets, namely involving the calculation of upper limits for the frequency of stars which are host to extrasolar planets at particularly wide orbital separations.

The suggestion is that the upper limits currently applied in context of the microlensing results may be underestimated, implying that planets at wide separations from their stars are actually more frequently-occurring than is commonly considered. This seems a reasonable consideration, as *Sumi's* search limit of 10AU for a host star would (in relative solar terms) approximately be only as far as Saturn, whereas Neptune exists in orbit around our sun at approximately 30AU. It would follow that a higher upper limit implies that more of the planets detected in the relevant microlensing studies may potentially be bound to stars at wider orbital separations, thus reducing the overall *Sumi* estimations of unbound planets roaming the galaxy.

An additional argument into the formation and thus population of unbound planets which may contend with these investigations comes from *Veras et al*^[23] (also in 2012) regarding the mechanism for generating the unbound planet population, questioning the planet-planet scattering and subsequent ejection of planets in main sequence planetary systems.

D. J. Stevenson^[24] outlines that during planet formation, Earth-mass objects consisting of rock and ice may be ejected from the system as they are scattered due to the gravitational influences surrounding the more giant neighbouring planets. *Veras et al* demonstrate that the planet-planet interaction process of ejection may not represent the only method by which the population of unbound planets may have arisen, the overall implication being that other potential sources of unbound planets, such as 'planetary stripping' in stellar clusters, may also contribute.

Regardless the formation process, the question is almost automatically raised as to the significance of an unbound planet in terms of one of the main goals of the overall extrasolar planet search; the question of habitability.

Stevenson^[24] had theorized several years earlier in 1998 that some planet-sized objects which drift within the galaxy (unbound to the heat and energy of a host star) could possibly maintain a dense enough atmosphere which would not suffer from heat loss in space. For example, *Lissauer et al (1987)*^[25] state that during the formation of planets, small-massed objects may be ejected from the system, and the resultant minimal exposure to their host's UV could allow a planet's hydrogen and helium rich atmosphere to be contained.

Stevenson calculates that for an approximately Earth-type object, geothermal energy from residual planetary core radioactivity would be capable of heating its surface to above the melting point of water, and so interstellar planetary bodies with oceans may well exist and even remain geologically active for long periods, where oceanic volcanism could provide sufficient energy for life.

Though Stevenson suggested a general disagreement at the time of his publication, the recent research of *Abbot & Switzer*^[26] (2011) indicated that an unbound planet with such an atmosphere may in fact be detectable, as they calculate in the case of Earth that reflected solar radiation could be detected up to a distance of 1000 astronomical units from our planet. And so for Abbot there is a concurrence with Stevenson on the possibility of life forming on an unbound planet (whether or not life previously or continued to exist at an earlier stage in the planet's existence) on the basis of underwater volcanic action, where they call on the work of *Baross and Hoffman*^[27] (1985) on the potential origins of life on Earth, which may have in fact developed in the vicinity of hydrothermal vents.

A further aspect of the habitability of unbound planets (the detection of which was predicted to be assisted by gravitational microlensing) was raised by *Debes and Sigurdsson*^[28] in 2007. They investigated the planet-planet scattering process to include not just the interactions between gas giants and Earth-sized planets, but also such earth-sized planets which were orbited by natural satellites similar to our own moon. Their simulations indicate that 5% of such planets with satellite companions will likely be ejected into interstellar space with the companion still gravitationally bound to the planet. On the question of habitability, the satellite is said to be capable of providing heating for the planet in the form of geological tidal heating, and could play as important a role as our own moon does to Earth.

As with many questions in the vast nature of astronomy, one is bound to the paradigm that given sufficient time, if enough (or all) of these outlined factors are in the ideal circumstances, life on an unbound planet is a curious concept, and a fascinating possibility.

2.4.3 A Cosmic Double Split Experiment

It is important to consider that microlensing is not by any means a tool which is limited to the detection of extrasolar planets; the phenomena of light being deviated by gravitational influences on a cosmic scale may hold the answers to a great many questions - both fundamental and abstract.

One speculative, yet possible *cosmological* application of gravitational microlensing is the intriguing notion of a massively scaled up testing of a variation upon "Young's double slit experiment", such that the gravitational microlensing effect between two stellar objects (such as a quasar and a galaxy) aligned with Earth will bend the rays of light around the lens-object towards the observer having been split into multiple trajectories, much like that seen in an interferometer. John Wheeler's^[29] thought experiment "delayed choice variation" of the double slit experiment states that the arrival of a photon at an observer has a choice of paths, which can lead to the determination (via measurement by half silvered mirrors) of which path the photon has travelled, or whether it travelled both rays as a wave.

In the example of a quasar which could be many millions of light years away, there is still the suggestion that with sensitive enough equipment, the photon may be forced to choose its path to earth from hundreds of millions of years into the *past*. Presently, groups at SETI (The Search for Extra Terrestrial Intelligence) are developing a conceivable test of the theory (Doyle, 2005^[30]). In 2007 Jacques et al^[31] proved that the act of observation itself in the experiment essentially determines whether the photon behaves as a particle or as a wave, thus verifying Wheeler's original thought experiment.

Furthermore, the concept lays the possibility of measuring the minimum time which is required for a light wave to emerge instead as a particle, supposing it is not (as is widely assumed) instantaneous. The example is considered whereby a distant quasar producing an interference pattern which is formed by a probability wave traversing two paths. Increasing the band-pass until the wave is seen as a photon would allow the rate of 'transition' from wave to particle to be calculated as proportional to the distance of the quasar per unit of time of band-pass increase.

This type of experiment represents important implications for the future applications of gravitational microlensing. For example, for lenses which do not cause a large variation in brightness, measuring the time delay in the light paths could be used to more accurately and directly measure the Hubble constant (that is, the Universe's rate of expansion).

3.0 Microlensing: Fitting, Improving & Simulating

The following sections discuss key aspects of researching gravitational microlensing events; gathering raw data by observation, fitting suitable models to the event data, and simulating theoretical data (such as event scenarios or photometry) in order to test various parameters. The investigations of these aspects demonstrate in a cyclical fashion how firstly, the raw data must be of the best quality, which may be achieved by improving the imaging techniques themselves. Secondly, the model fitted to the raw data must be accurate and dynamic in order to obtain the most precise event parameters such as planetary characteristics (of course, the model will improve with improved quality in raw data). In addition, theoretical simulations of improved imaging techniques will demonstrate in detail to what extent the raw data quality may be improved.

3.1 Fitting Microlensing Data

As previously indicated, an important task for any microlensers to undertake is to firstly demonstrate an understanding of the mathematical (and overall) theory, before learning the essentials of statistical analysis and computational simulations in order to be able to quickly and effectively model a microlensing event's lightcurve from raw data. The following steps illustrate an example of this procedure using the theory outlined in *section 2.3* above.

3.1.1 Data, Errors and Suitable Models

The raw data points of a microlensing event light curve produced by observations made by OGLE are shown with errors, exemplifying the typical magnification seen when a source and lens star are aligned with the observer. In order to characterise the data points and establish relevant parameters, a basic magnification model was drawn purely for comparison, see *figure 8*.

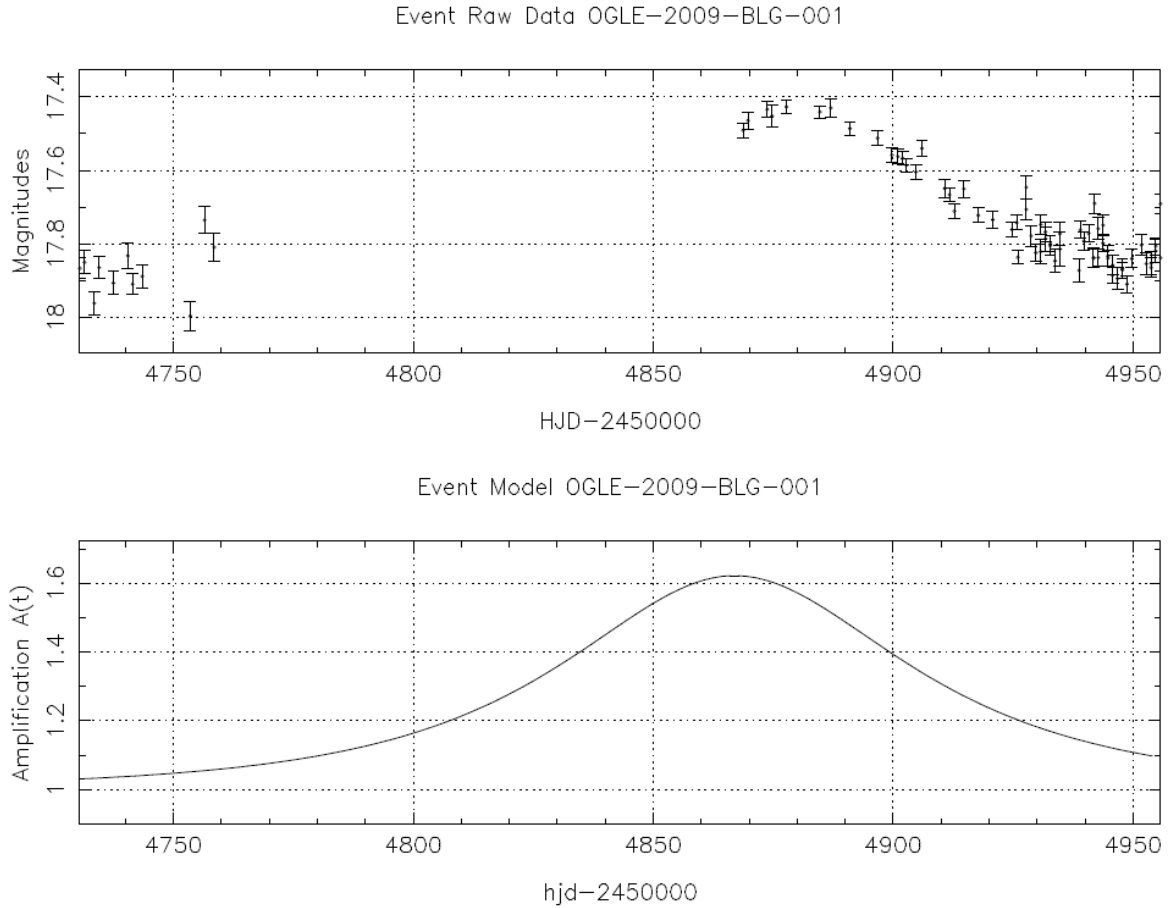


Figure 8 - Top: OGLE raw data points with error bars for a typical microlensing event, note that there are often significant gaps in the data due to the unpredictable nature of events and disturbances in observing, however it is the nature of model-fitting which overcomes such problems. **Bottom:** A basic PSPL model generated in full using the timescale and other parameters provided by the observational data.

In order to fit the data to the model correctly, firstly a conversion must be made given that the model is given as a magnification factor A , whereas the data points are given in magnitudes m with regard to some offset m_0 , and thus it is more appropriate to work in units of flux, F

$$F = 10^{-0.4(m-m_0)} \quad (9)$$

Given that the error bars of the data σ_m are also reported in magnitudes, it is also necessary to carry out error propagation in order to determine the error bars in terms of flux, σ_F

$$\sigma_F = \sigma_m \left(\frac{dF(m)}{dm} \right) \quad (10)$$

In order to fit the data in (units of flux $F(t)$) to the model (in units of magnification $A(t)$), the relationship must be made which becomes more accurate when incorporating the source flux F_S and the blend flux F_B (the flux of non-lensing stars which are unresolved on the image) into the more suitable model

$$F(t) = F_S A(t) + F_B \quad (11)$$

The values of the model's magnification were plotted against the observed OGLE flux data values in order to determine their dependence, *see figure 9*.

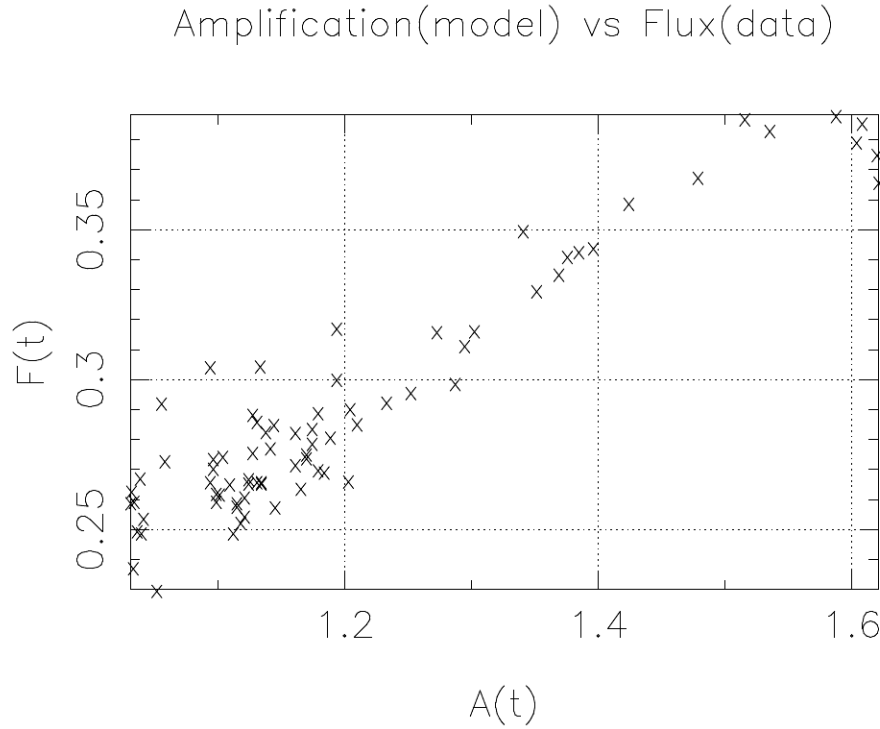


Figure 9 - The fluxes F of the raw OGLE data are plotted against the magnification factor A produced by the model, where linear regression equates the model equation $F(t) = F_S A(t) + F_B$ with the equation of a linear fit $y = mx + c$ (gradient m and intercept c)

Linear regression analysis was performed on the resulting trends, whereby in a linear fit, the intercept is now the blend flux and the slope is the source flux. Applying this for linear regression, the dependency of A on F is related through the newly propagated flux errors σ_F in order to give the blend and source fluxes^[32]

$$F_S = \frac{\sum \frac{A(t)F}{\sigma_F^2} \sum \frac{1}{\sigma_F^2} - \sum \frac{A(t)}{\sigma_F^2} \sum \frac{F}{\sigma_F^2}}{\sum \frac{[A(t)]^2}{\sigma_F^2} \sum \frac{1}{\sigma_F^2} - \left[\sum \frac{A(t)}{\sigma_F^2} \right]^2} \quad (12)$$

$$F_B = \frac{\sum \frac{[A(t)]^2}{\sigma_F^2} \sum \frac{F}{\sigma_F^2} - \sum \frac{A(t)}{\sigma_F^2} \sum \frac{A(t)F}{\sigma_F^2}}{\sum \frac{[A(t)]^2}{\sigma_F^2} \sum \frac{1}{\sigma_F^2} - \left[\sum \frac{A(t)}{\sigma_F^2} \right]^2} \quad (13)$$

These newly determined values are then used to complete the fitting of the data to the model, which may now be expressed in preferred units of flux (or by simple conversion, magnitude). The results of this fit may be compared with the fit given independently by the OGLE team, *see figures 10 and 11*.

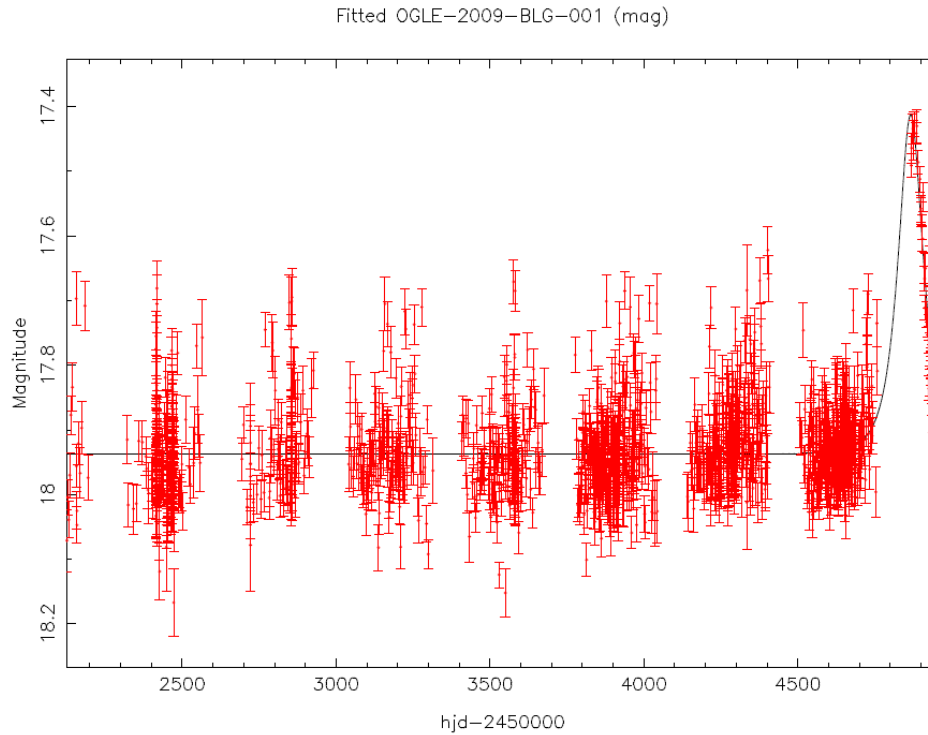


Figure 10 - The newly constructed computational model is fitted to the original OGLE data points for comparison with the OGLE team's own fit, *see figure 11*, and is in-keeping with the typical Paczyński light curve outlined in *section 2.4*

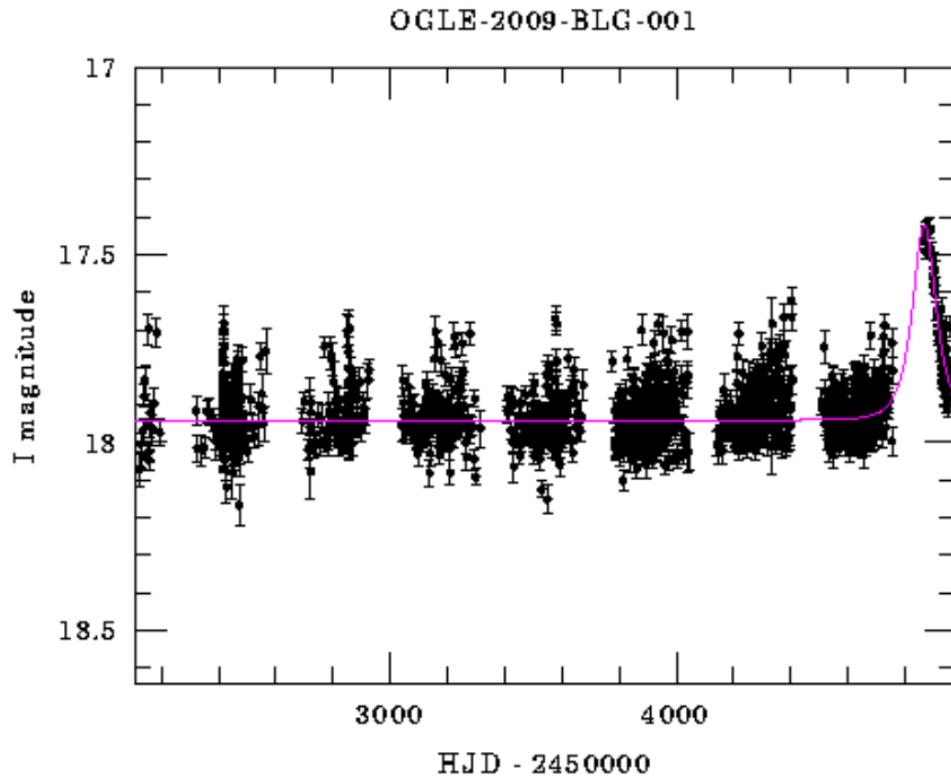


Figure 11 - The original OGLE data which has been fitted using OGLE's own fitting methods, in comparison with the newly fitted model found in *figure 10*. Taken from the OGLE project pages^[41]

As can be seen, the computational modelling process has successfully improved what was originally a very general and rough lightcurve to the data (*figure 8*), to a dynamic fit which follows the data points more suitably (*figure 10*). This has given rise to a marked improvement in the scatter of the data points, as in the case of OGLE's own fitting regime (*figure 11*), and thus this has served as a consistency check in the methodology of event-fitting.

The subroutines for this process may now be applied relatively universally to any dataset for a given microlensing event, and thus members of various global teams may now compare and contrast their findings, as is essential in this area of research.

3.2 Optimising the Data Selection

3.2.1 The Reductions Pipeline

Given that raw data from the various observatories may now be locally modelled both quickly and effectively, it is important to be able to monitor the quality of the data and the fitting of a microlensing event as it enters the automated pipeline system in the RoboNet project pages, namely the reductions section of the pipeline^[54]. As such this section describes systems which may be put in place to ensure only the highest quality data is used in computing event light curves, ultimately determining planetary candidates and their characteristics. That is to say, the ability to fit a model to data is predicated on the data being sound and of good quality, and as such careful steps must be taken to ensure this.

The reductions pipeline is set up such that as exposures are taken of a reported microlensing event, the images of the target and their accompanying photometric data are stored in a stack, which may originate from any of three telescopes using the webPLOP Observation Prioritisation System^[55]; the Liverpool Telescope (LT) on La Palma in the Canary Islands, the Faulkes Telescope North (FTN) on Haleakela in Hawaii and the Faulkes Telescope South (FTS), at Siding Springs in Australia.

In order to accurately determine the relative change in magnification during a microlensing event, the system uses an inbuilt algorithm to select the most ideal (typically the sharpest) 'template image' based on the available photometric data^[56]. The model fitted to all images is a *sky background* (accounting for changes in sky brightness due to clouds, the phase of the moon etc.) plus the template, which is *shifted* (accounting for the change in telescope pointing; moving the target from one pixel to another on the CCD), *blurred* (accounting for changes in the seeing), and *scaled* (accounts for changes in transparency of atmosphere). Subtracting the fitted model gives a difference image for each original image, which has effectively removed all constant stars, leaving only the PSFs (point-spread function) of variable stars, in particular the target event. The change in flux is estimated here by optimal scaling of the PSF model to fit these residuals, and essentially the light curve of the event may be drawn.

However in order to select the 'ideal' template image, several important primary and secondary selection factors must be considered, which are listed alongside each image in the pipeline.

Primary Factors include:

- A low FWHM (full-width at half-maximum) is the primary factor for selection as a template image; the lower the FWHM, the sharper the image, and therefore the more effectively it can be blurred to match the images.
- A predefined Sky Brightness threshold which may not be exceeded

Secondary factors include:

- A generally low sky background, which may increase due to clouds or moonlight.
- A high photometric scale factor, which is the ratio of star signal of one image to that in the reference image. This depends on the air-mass and the clouds through which the image was taken.
- A low Air-mass, which is the number of atmospheres of air through which the target is observed (i.e. 1.0 for looking at the zenith)
- Round images, given that distorted images in the template will lead to poorer reductions.
- A faint target, as this results in less photon noise near the target, and thus ideally there should be no saturated images near the target either, *see section 3.3.1*

However, the system is set up such that the template image is selected based on the images available at the time of reduction, and given that events may occur over many days, many factors (such as those outlined above, as well as rare technical glitches) may lead to a less than ideal image being selected. As such, over one hundred microlensing events undergoing automatic reduction were carefully monitored, and the software's choice of template was scrutinised manually for each. This is an important consideration, as the choice of template image ultimately decides the accuracy of the reduction, and hence the quality of the final light curve.

Typically this would involve cross-referencing the automatically chosen template with other available images (anywhere from a few to several dozen per observing telescope) which have made up the light curve, cross-referencing the image parameter values, and considering whether there are any with better numerical characteristics, or indeed any with targets in better circumstances (i.e. fainter, with rounder images or without nearby saturated objects). If a better image exists, a basic reset of the reduction pipeline is initiated, which will simply repeat the same process in the hope of recognising the better choice (which may have been missed if it was a very recent exposure for example). If this does not improve the light curve, this action may be undone, and the preferred template image is selected manually for use during the reduction reset.

An example of this may be seen for "MOA-2011-BLG-0093_FTS" (i.e. MOA event #0093 from 2011, with images taken by the FTS towards the Galactic Bulge). Initially a template was automatically chosen with $FWHM = 1.549$ to produce the light curve, *see figure 12*, when several significantly sharper images existed.

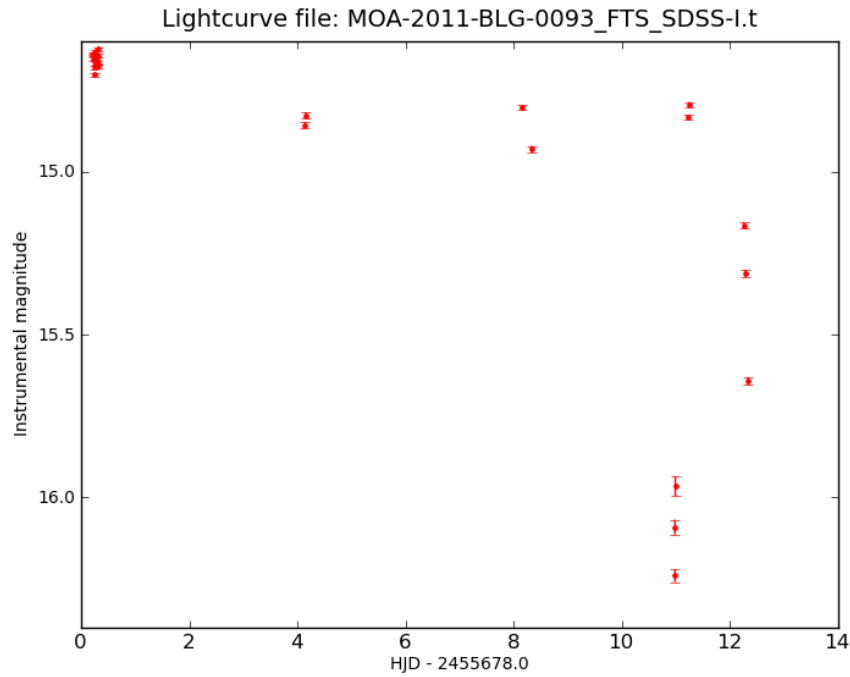


Figure 12 - This light curve was created using a poor template image chosen by the software, resulting in highly skewed magnitude data points on the light curve, which would be difficult to fit a model to.

Following a reset, the re-reduction resulted in the choice of a far sharper template image, in this case with lower sky and far improved (59.2%) lower $FWHM = 0.973$, see figure 13.

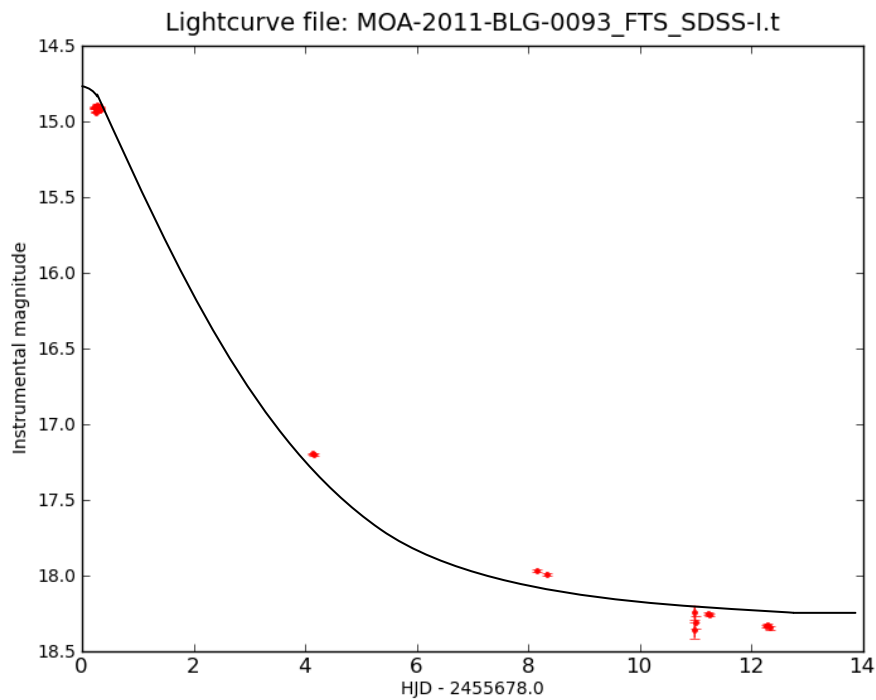


Figure 13 - Post 're-reduction', the light curve for the same event's newly produced data points has vastly improved, exhibiting the typical shape with a microlensing t_0 peak at closest alignment, converging on a baseline, as per a Paczyński curve, as seen in section 2.4

This has resulted in a far more accurate light curve whose data points agreed with and contributed more realistically to the rest of the collaborators who were observing the event. It is important to note that in extreme and critical cases, this type of attention to detail could mean the difference between detecting a planet, accurately determining its characteristics, or overlooking one entirely.

3.2.2 Further & Future Improvements

A number of adjustments and enhancements may be made to the working pipeline in order to improve its choice of template image for reductions. A model which definitively prioritises the characteristics of the ideal template image with respect to all images would be the first step. The early stages of an investigation into the selection habits of the software was begun, whereby any of the listed factors may be compared. For example, the FWHM and sky of each image in an event were plotted against each-other, *see figure 14*. The original automatically selected template image *A* was then highlighted, followed by the preferred manually selected template image *M*, and repeated for a number of events.

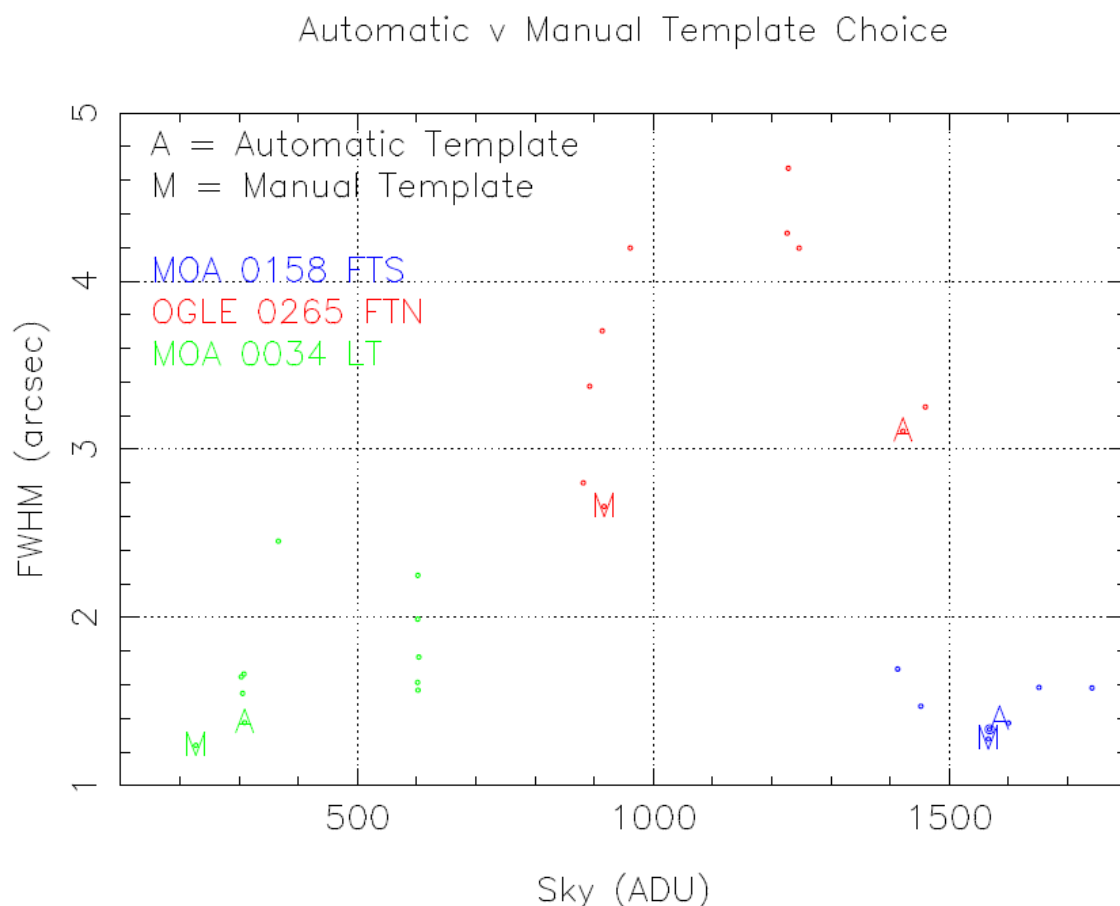


Figure 14 - A first look at the consistency of the automatic (**A**) selection of the template image shows that typically there are sharper images with lower sky backgrounds available, which were manually (**M**) selected for each event.

Further investigation may cross-reference all selection criteria and determine a simple change required in the reduction pipeline's algorithms.

Another improvement would be to formulate an appropriate metric and use it to implement a code which automatically produces a ranked list of candidate template images from those available, and then trigger appropriate reprocessing when significantly better candidate template images become available. This would significantly simplify the workload and potentially remove the need for extensive human monitoring outlined above, in order to keep the real-time reductions up to date.

Finally, the pipeline is currently run separately both for each telescope and each filter combination. Essentially this means usually there are at least three stacks of data being separately reduced for each event and applied to the model. As such it would be beneficial to investigate the option of setting up the pipeline to combine data in the same filter from different telescopes, meaning the best overall template image could be selected regardless of which telescope it was taken from, and used to analyse the data from all feeds as a whole, leading to more realistic data points for the light curve.

In order to investigate and implement such improvements, a version of the pipeline may be taken offline and events and their reduction algorithms can be safely analysed without affecting their current status.

3.3 Microlensing Photometry: Improvements from Theory

Whilst ensuring that the best quality of available exposures is selected for analysis, and fitting a high quality and realistic model to the data points are both essential steps in these types of investigations, another important aspect to improve upon is the gathering of that original raw data itself; that is, ensuring that the imaging process results in original exposures which will give rise to the best photometric data.

Lucky imaging as an astronomical imaging technique has been developed since the mid twentieth century, and is a somewhat counter-intuitive method of stacking very short-exposure images to form a final image with markedly improved quality, due to the reduction in unwanted exposure of astronomical seeing conditions such as the Earth's turbulent atmosphere. Recently in 2007, the method was combined with adaptive optics at Caltech and Cambridge University to achieve up to 0.025 arcseconds resolution, which was close to the theoretical limit of their 200-inch Hale Telescope and at the time was the greatest resolution obtained by direct imaging from Earth, even out-performing the Hubble Space Telescope. Essentially, lucky imaging has the potential to reduce the need to send telescopes into space in order to overcome atmospheric seeing-effects, saving great time and expense.

3.3.1 Lucky Imaging Signal to Noise Ratio

Astronomical Seeing Conditions are those which perturb and deviate the course of a wavefront en-route to a detector on Earth^[34]. These include clouds, light pollution and atmospheric turbulence, which is the natural motion of the layers of the Earth's atmosphere due to the heat exchanges caused by the weather. As the signal from space passes through the turbulence, the signal itself becomes perturbed and turbulent, *see figure 15*, leading to an image such as a star breaking up into various speckles which vary over time; this is the scintillation (commonly known as the 'twinkling') of stars. *See Section 3.3.3 which includes a simulation of this effect.*

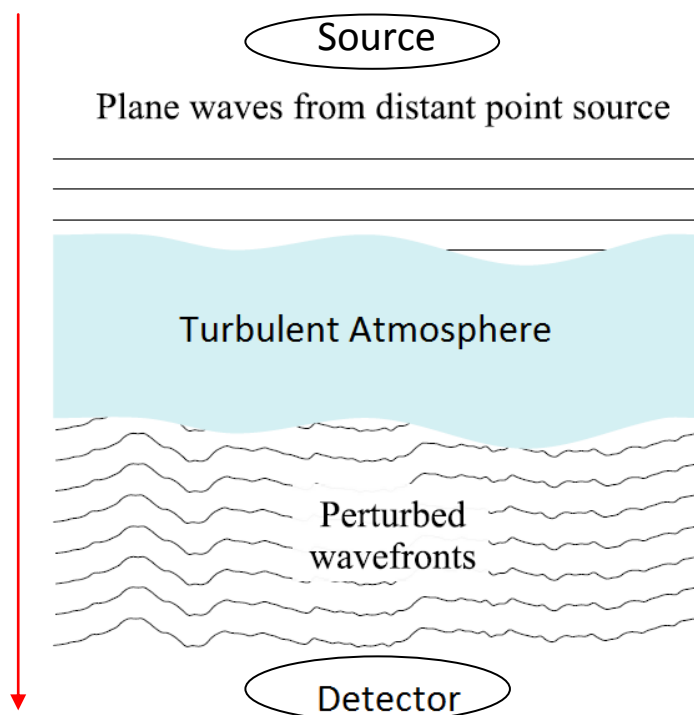


Figure 15 - An illustration of how plane waves from a point source (such as a star) in space enter Earth's turbulent atmosphere, and become perturbed as a result of the changes in refractive index before detection at the surface. Diagram adapted from R. N. Tubbs' thesis, 2003^[35]

Lucky imaging^[36] is a type of speckle imaging^[37] which uses a high-speed camera to take a large number of extremely short exposures, so that the effects of changes in the Earth's atmosphere over time are avoided. This results in the typically *seeing-limited* photometry of standard imaging effectively converging on *diffraction-limited* photometry, and thus with sufficient precision and technology is potentially comparable with photometry directly from space.

The sub-second exposures are sorted by their quality (such as their Strehl Ratio^[38]; the peak value of the PSF compared with that of purely diffraction-limited imaging), of which some percentage (typically 1%-10%) of those least affected by the atmosphere (i.e. the sharpest) are selected for combination into one single image by 'shifting and adding', yielding much higher resolution than would be possible with standard images taken with long exposure

times, because the star images in the short exposures are effectively aligned to the brightest speckle before co-adding. Using this method, the resulting lucky point-spread function is comprised of a diffraction-limited 'core' (depending on the quality of the primary mirror) to which some fraction f of the total photons contributes, and a seeing-limited 'halo' contributed to by the remainder $(1-f)$, where the halo corresponds to the superposition of the un-aligned sub-dominant speckles. The core fraction f thus increases as the percentage of exposures used in the stack decreases; more exposures in the stack leads to more variation in the final image and thus more contribution to the halo, and as such the ideal number of exposures is very low and all must be of very high quality in order to converge on the idealised value $f = 1$; an exposure comprised entirely of the sharp core, with no halo. The objective of this study was to determine how much improvement in the photometry can be gained with lucky imaging over standard imaging, namely in terms of the potential increase in signal to noise ratio (S/N).

Though typically Gaussian (or Moffat) functions are used for more realistic PSF constructions, in order to obtain very basic analytical results, boxcar (uniform) PSFs were first adopted to approximate that of standard imaging techniques, and also for that of lucky imaging with a core-halo structure, *see figure 16*, with a fraction f of the photons in the core and fraction $(1-f)$ in the halo. In this regime it follows that $f=0$ for standard imaging (i.e. all light is distributed in the typical seeing-limited halo, and thus the lucky PSF would be equivalent to the standard PSF), and $f=1$ for diffraction-limited imaging (i.e. all light is concentrated in the core, as can be expected in photometry from space). As such we expect $0 < f < 1$ for lucky imaging, and set out to investigate the consequences of various scenarios.

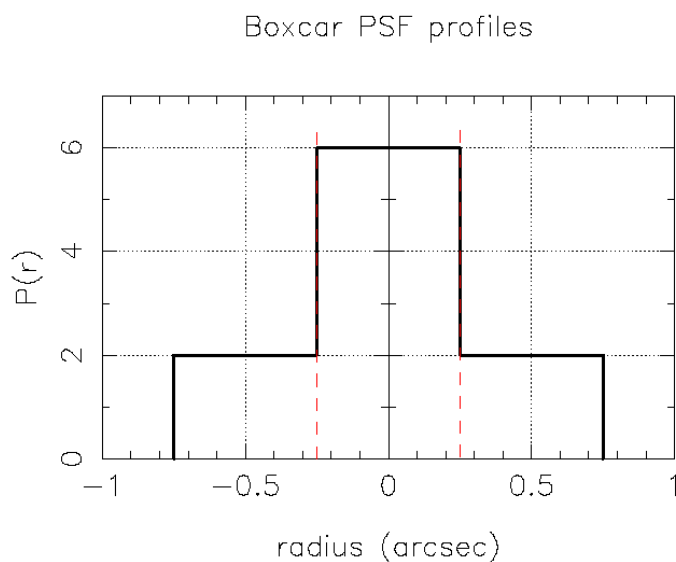


Figure 16 - For basic analysis, a boxcar (uniform) PSF shape was chosen for the lucky PSF, where the more intense 'core' has a fraction f of the photons, giving way at the marked boundaries to the outlying 'halo' which has a remaining fraction $1-f$ of the photons. For comparison, a standard-imaging (boxcar) PSF is assumed to be equivalent to the lucky halo PSF alone (i.e. when $f = 0$, full photon contribution to the halo)

For a typical diffraction-limited (d) telescope of diameter $D = 1.0\text{m}$ observing light of wavelength $\lambda = 800\text{nm}$, the resolution is given by the standard deviation $\sigma_d = \frac{\lambda}{D} = 0.165$ arcsec. The typical seeing-limited (s) standard imaging has $FWHM = 1$ arcsec seeing, corresponding to $\sigma_s = 0.424$. The ratio of seeing-limited to diffraction-limited imaging is therefore usefully defined by the parameter $x = \frac{\sigma_s}{\sigma_d} = 0.39$, such that $x=0$ for very bad seeing, and $x=1$ for 'perfect' seeing conditions.

In order to determine the improvement in S/N , $data \mu_i$ and $noise \sigma_i$ models were adopted for data D_i , with RMS readout noise σ_0 , gain G and background flux B for some PSF, P

$$\langle D_i \rangle = \mu_i = f_* P_i + B \quad (14)$$

$$\sigma_i^2 = \sigma_0^2 + \frac{\mu_i}{G} \quad (15)$$

Optimal photometry determines the flux f_* of a star by optimal scaling of the PSF P to fit the data, given by the following dot product ratio

$$\hat{f}_* = \frac{(D-B) \bullet P}{P \bullet P} \quad (16)$$

Where some general dot product $A \bullet B$ may be defined as

$$A \bullet B = \sum_{i=1}^N \frac{A_i B_i}{\sigma_i^2} \quad (17)$$

And where the variance of the flux may now be defined according to the inverse PSF dot-product

$$Var[\hat{f}_*] = \frac{1}{P \bullet P} \quad (17)$$

Generally the S/N is defined as the ratio of useful or meaningful information, the signal, to that of the unwanted background noise. That is the mean of the signal, i.e. the mean of the flux, to its standard deviation (the square root of the variance), such that $(S/N)^2$ may now be defined as

$$\left(\frac{S}{N}\right)^2 = \frac{\langle \hat{f}_* \rangle^2}{Var[\hat{f}_*]} = \frac{\langle (D-B) \bullet P \rangle^2}{P \bullet P} = f_*^2 P \bullet P = f_*^2 \sum_{i=1}^N \frac{P_i^2}{\sigma_i^2} \quad (18)$$

And thus we have an expression for the general S/N improvement of photometry with some defined PSF P , where all factors are considered for an accurate representation

$$\left(\frac{S}{N}\right)_{General}^2 = f_*^2 G \sum_{i=1}^N \frac{P_i^2}{\sigma_0^2 G + B + f_* P_i} \quad (19)$$

It is convenient to break this expression down into two simplified cases; In the case of very bright stars, i.e. very high flux with respect to background noise, the minor background factors may be neglected, and thus the expression reduces

$$\left(\frac{S}{N}\right)_{Bright}^2 = f_* G \sum_{i=1}^N P_i \quad (20)$$

Conversely, in the case of very faint stars, i.e. very low flux with respect to the background noise, the expression reduces such that these factors dominate

$$\left(\frac{S}{N}\right)_{Faint}^2 = \frac{f_*^2 G}{\sigma_0^2 G + B} \sum_{i=1}^N P_i^2 \quad (21)$$

An interesting point of note is the point at which the flux of both the faint and bright S/N are equal, defined as a transitional point in either regime in order to account for the cut-off definition of each:

$$f_{* transition} = (\sigma_0^2 G + B) \frac{\sum_{i=1}^N P_i}{\sum_{i=1}^N P_i^2} \quad (22)$$

The faint and bright S/N cases are plotted with increasing flux, along with that of the general S/N expression, *see figure 17*, where the S/N when considering bright and faint limits separately can be seen to meet at the marked transition point. This is a reasonable approximation of the behaviour of S/N with increasing flux, however the general expression's curve shows more realistically how the trend would rise similarly with the faint limit at lower fluxes, before diminishing to converge with the bright limit after the marked point of transition towards brighter fluxes.

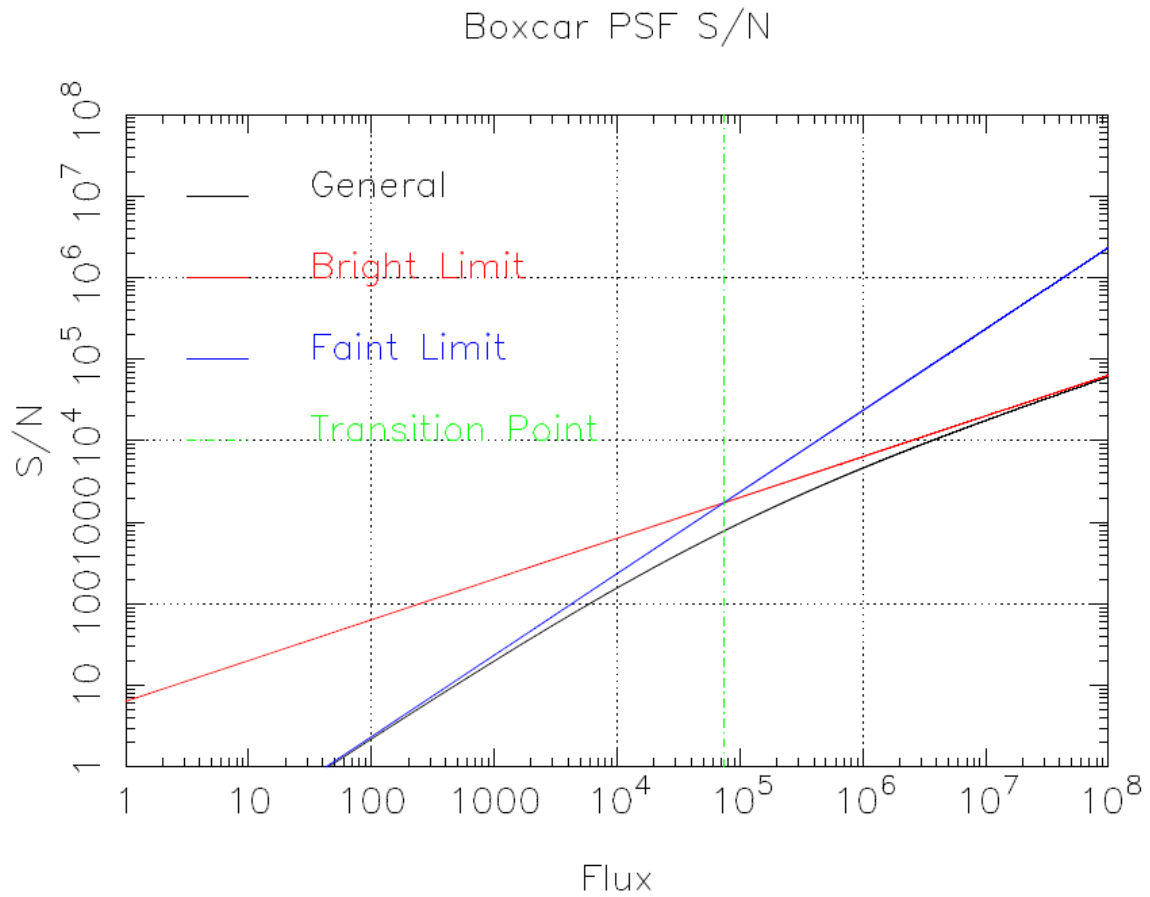


Figure 17 - The bright (red) and faint (blue) limits of the S/N are seen to be reasonable approximations to the general (but complex) expression for S/N with increasing flux, while the marked transition point serves as an estimate for the theoretical changeover in regimes.

When taking into account the nature of the bright and faint limit expressions, it is seen that on a logarithmic plot the S/N improvement will have double the slope in the faint limit, and so after the transition point this becomes an unreasonable approximation by comparison. However, taking the faint limit prior to the transition point and the bright limit after the transition point is an overall reasonable approximation to the more complicated general case.

The improvement factor ε of lucky photometry (L) over standard photometry (S) may now be defined as the ratio of their respective S/N

$$\varepsilon^2 = \frac{(S/N)_L^2}{(S/N)_S^2} \quad (23)$$

And so in the bright-star limit there is no improvement, given that for exceptionally bright targets the noise levels are rendered insignificant, whereas in the faint-star limit the S/N improvement factor will depend on the PSF, and hence on both the factors f and x .

An estimate for the relationship between f and x would assume that all speckles have equal brightness, and thus if the number N of speckles as previously defined is given by $N \sim \left(\frac{D}{r_0}\right)^2 = \frac{1}{x^2}$, and each speckle has a certain fraction of the light $\frac{1}{N} \sim \frac{1}{x^2}$, then equating this with photon fraction f above reveals a proportional variation $f \propto x^2$.

Taking the faint limit of S/N into consideration for simplicity, and using a boxcar PSF shape for standard imaging P_S , and boxcar PSF shape for lucky imaging P_L with respect to its radius from centre r , we have

$$P_L(r) = f \cdot P_C(r) + (1 - f) \cdot P_H(r) \quad (24)$$

Where P_C and P_H are the PSF's of the individual core and halo components respectively, which contribute towards the overall lucky PSF depending on the photon contribution to the core, f .

Synthesising datasets and their plot of ϵ^2 varying with increasing x^2 shows a peak in improvement at $\epsilon^2(x) = 1.25$, thus the improvement factor is $\epsilon = \sqrt{1.25} \sim 1.118 \sim 11.18\%$ in *lucky imaging* over *standard imaging* for boxcar PSF shapes, see figure 18.

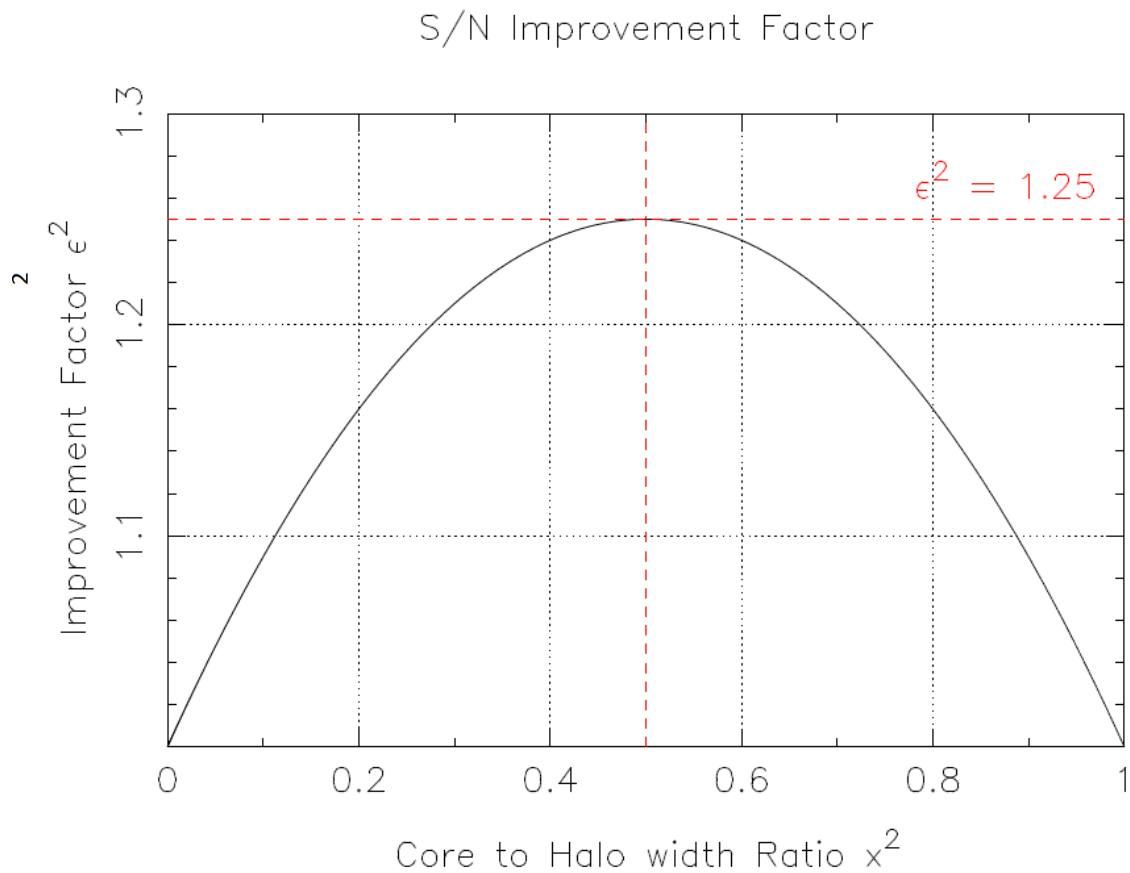


Figure 18 - The improvement factor of lucky to standard imaging ϵ varies as a parabola with the core to halo width ratio x , such that a peak improvement is found at $x \sim 0.707$, and at $\epsilon = \sim 11.18\%$

Though $\sim 11\%$ improvement is a fairly modest initial result, it is based only on a highly rudimentary PSF shape (boxcar). It has however outlined the essential analysis required, which was then adapted for a more realistic PSF shape.

The standard seeing-limited PSF P_S is now instead considered a symmetrically circular 2D Gaussian (as is often adopted as an accurate construction of typical PSFs) with standard deviation $\sigma_S = 0.424$ for 1 arcsec of seeing, as previously defined

$$P_S(r) = P_{S0} \cdot e^{\left(\frac{-r^2}{2\sigma_S^2}\right)}, \quad P_{S0} = \frac{1}{4\pi\sigma_S^2} \quad (25)$$

Where P_{S0} is the normalisation factor for the PSF at peak intensity (radius $r = 0$). This is now comparable with a "lucky Gaussian PSF" P_L , once again of the core and halo form

$$P_L(r) = f \cdot P_C(r) + (1 - f) \cdot P_H(r) \quad (26)$$

Where PSFs P_C (the lucky core) and P_H (the lucky halo) are now also symmetrically circular 2D Gaussians whose contributions to the overall PSF are determined by the fraction of photons in the core f , and are given for fullness in terms of their respective standard deviations; $\sigma_H = 0.424$ comparable to seeing-limited imaging, and $\sigma_C = 0.165$ comparable to diffraction-limited imaging

$$P_H(r) = P_{H0} \cdot e^{\left(\frac{-r^2}{2\sigma_H^2}\right)}, \quad P_{H0} = \frac{1}{4\pi\sigma_H^2} \quad (27)$$

$$P_C(r) = P_{C0} \cdot e^{\left(\frac{-r^2}{2\sigma_C^2}\right)}, \quad P_{C0} = \frac{1}{4\pi\sigma_C^2} \quad (28)$$

The more realistic Gaussian profile of the lucky PSF was plotted for comparison with the Gaussian standard imaging PSF for varied f , see figure 19, where $f = 1$ gives full photon contribution to the lucky core, giving the greatest intensity (the sharpness that may be expected from diffraction-limited photometry such as that from space), $f = 0.5$ gives equal contribution to both the core and halo, and $f = 0$ gives full contribution to the halo alone, and as can be seen is equivalent to the profile of a standard imaging PSF.

Gaussian PSF profiles

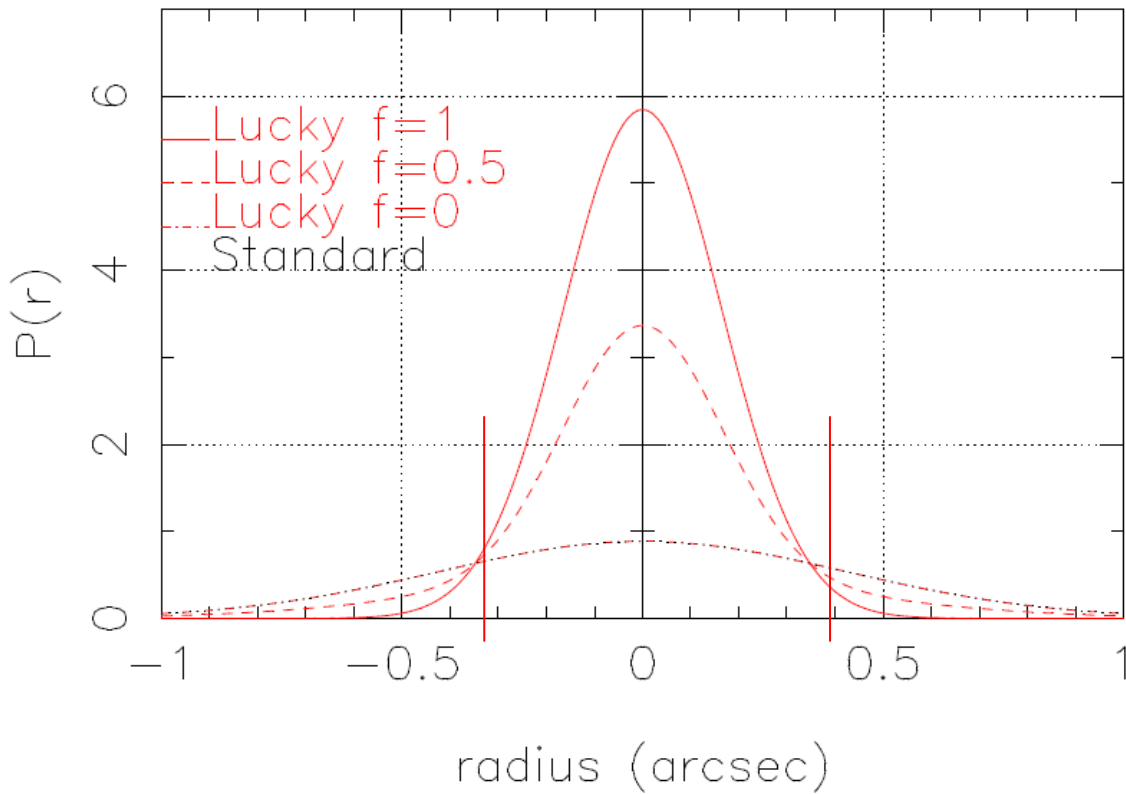


Figure 19 - The changing profile shape of the lucky PSF due to increasing photon contribution to the core f . The vertical boundary marks a useful definition of where the theoretical boundary between the core and halo may occur. When all photons are contained in the core, the PSF is at its sharpest with rapidly diminishing wings typical of diffraction-limited photometry, whereas full photon contribution to the halo results in a far less sharp PSF, typical of seeing-limited photometry.

When considering the boundary between the core and halo, a more theoretical approach was taken in comparison with the boxcar PSFs' simplified abrupt 'edges'. The boundary r_b is defined as occurring at the meeting point of the intensities of the extreme cases of the core and halo PSFs, conveniently in terms of their standard deviations, σ_H and σ_C

$$r_b = \pm \sqrt{\frac{\ln\left(\frac{\sigma_H^2}{\sigma_C^2}\right)}{\frac{1}{2\sigma_C^2} - \frac{1}{2\sigma_H^2}}} \quad (29)$$

The S/N of lucky imaging was then plotted in a similar fashion for varied values of f and compared with a standard imaging PSF, see *figure 20*. In order to carry this out computationally given the complicated nature of the general S/N expression, the integral which included both the PSF P and P^2 must be calculated for each value of $flux$. Given the further complicated nature of the Gaussian PSF, this could only be achieved numerically as part of the computer simulation, which coded the area under the distribution before plotting.

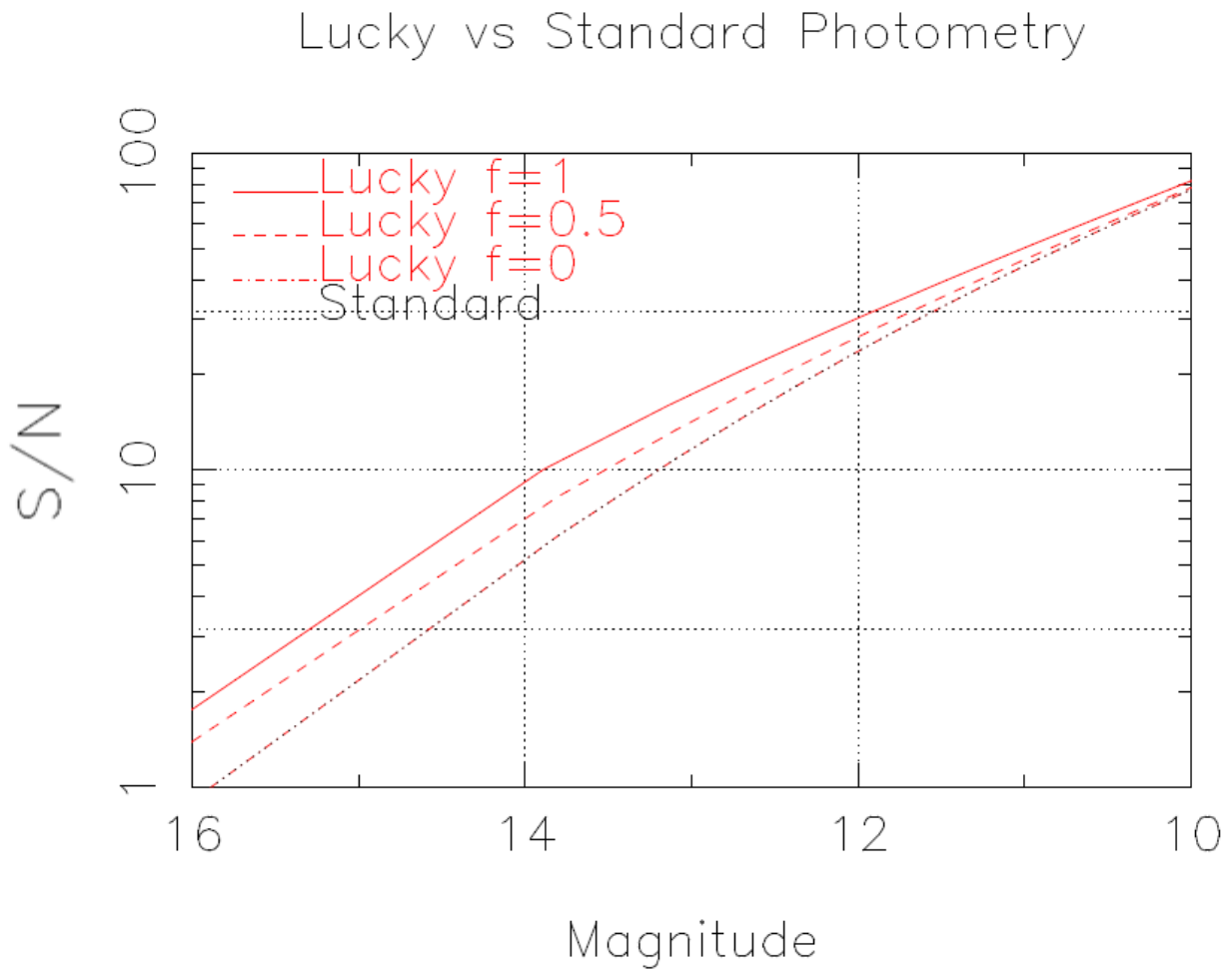


Figure 20 - As the fraction f of photons in the core increases to 1, the relative improvement in S/N for lucky PSFs increases, particularly in the faint limit, with less improvement for brighter stars. As expected, a value of $f = 0$ in a lucky image's S/N results in an identical trend to that of a standard image's S/N .

As the fraction f of photons in the core increases to 1, the improvement in S/N for lucky PSFs increases, particularly in the faint limit, with less improvement for brighter stars. This is particularly highlighted when the lucky PSF S/N is normalised with respect to the standard imaging PSF, see figure 21.

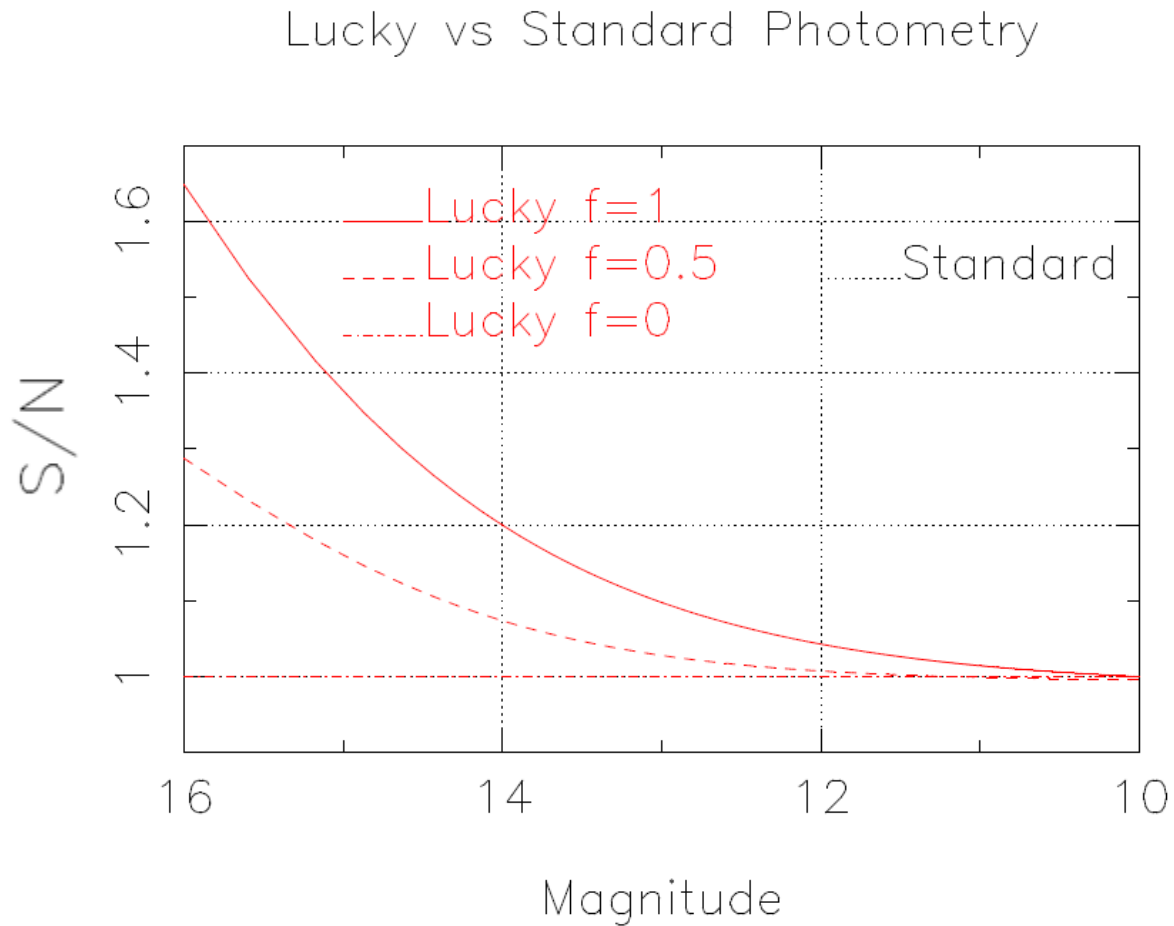


Figure 21 - The normalised plot shows how the lucky (Gaussian) PSF S/N is improved over standard imaging for varied fractions of photons in the core, particularly in the faint limit, with no improvement seen for higher magnitude stars; as expected from the outlined theory in the case of full photon contribution to the halo $f = 0$, the lucky imaging S/N is equivalent to standard imaging.

At the faintest limit, the lucky imaging regimes show a distinct improvement in S/N over the standard imaging; a maximum $\sim 60\%$ when $f = 1$, $\sim 25\%$ when $f = 0.5$ and as expected 0% when $f = 0$, however as the brightness increases and renders the noise components negligible, all regimes converge on the S/N improvement of that of standard imaging. Depending on the realistic value of $f > 0$, the improvement in the faint limit of a Gaussian lucky image is significantly higher in comparison with the $\sim 11\%$ increase found with the boxcar lucky image regime.

As with the simplified boxcar version of the PSF, the lucky Gaussian regime was also investigated to determine how the S/N improvement factor ε would vary with the core to halo width ratio x (where $x = 0$ represents very bad seeing, and $x = 1$ represents very good seeing) see figure 22. Given that the relationship between f and x is not clearly defined and sparsely alluded to in theory, a first step considered the relationship as $f = x^P$ where P is the unknown power dependency to be investigated, initially estimated between 1 and 2 as previously outlined above.

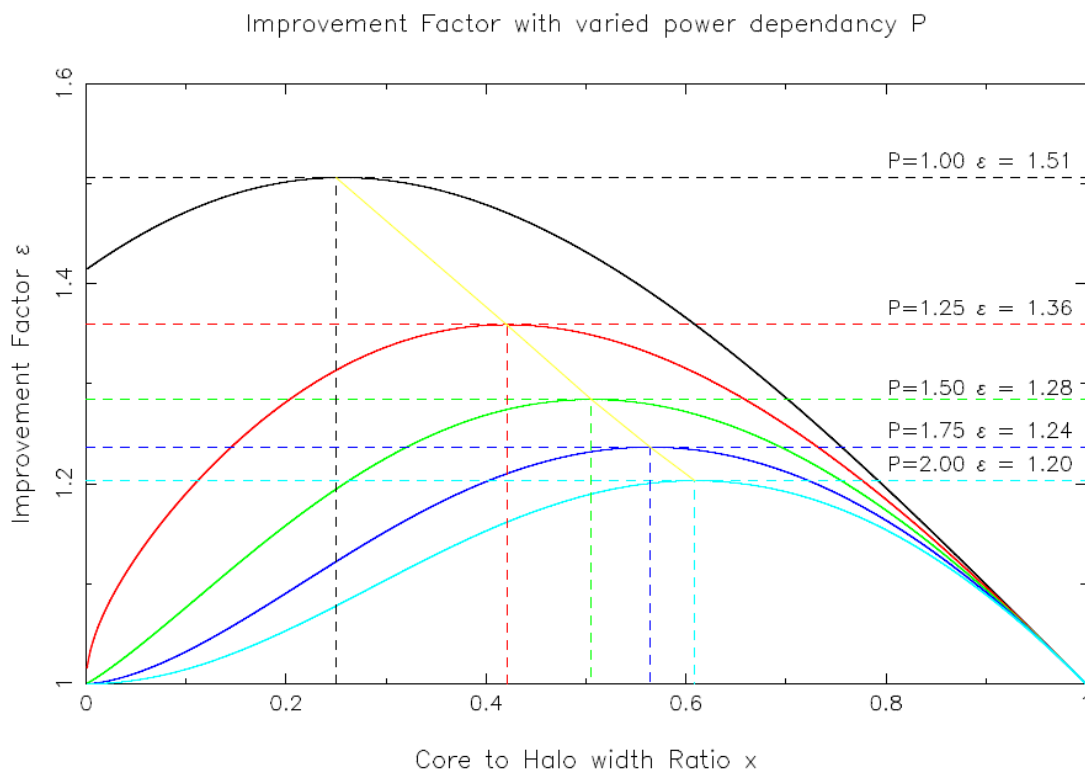


Figure 22 - The potential improvement ε of lucky imaging over standard imaging is illustrated for a range of possible $f = x^P$ relationships when a Gaussian PSF is adopted in the faint S/N limit. The peaks are identified with a *lower limit* of 20% improvement when $f = x^2$ (as was stipulated in the case of the simplified boxcar PSF model) and an *upper limit* of 51% improvement when $f = x$

A constraint of the improvement factor of lucky imaging over standard imaging may now be placed, indicating a lower limit of 20% improvement when $f = x^2$, and an upper limit of 51% improvement when $f = x$. The slight discrepancies found in the 25% and 60% values obtained above are a result of simplifying the case in figure 22 to only include the faint limit of S/N in order to illustrate the maximum benefit, as opposed to the more realistic general case S/N.

Therefore to extend the analysis of the dependence of f on x , three possible relationships were considered; $f = 0$ for a standard seeing-limited PSF, and $f = x$ and $f = x^2$ (that is for $P = 1$ and $P = 2$) for lucky PSFs, demonstrating the extremes in upper and lower limits identified above.

A useful measure of the quality of a PSF is the Strehl Ratio S ; the peak value of the PSF in relation to that expected from theoretical purely diffraction-limited imaging. In our case this is the peak value of the lucky PSF P_L relative to the peak value of the diffraction-limited core PSF P_C at radius $r = 0$

$$S = \frac{P_L(0)}{P_C(0)} = \frac{f P_{Co} + (1-f) P_{H0}}{P_{Co}} = f + (1-f) \frac{1/4\pi\sigma_H^2}{1/4\pi\sigma_C^2} \quad (30)$$

Replacing for x , this gives

$$S = f + (1-f)x^2 \quad (31)$$

The Strehl Ratio may now be parameterised as $S(x,f)$, see figure 23. In this regime, $f = 0$, x and x^2 are overlaid with contours of S with values ranging from 0 to 1.

Strehl Ratio Contours

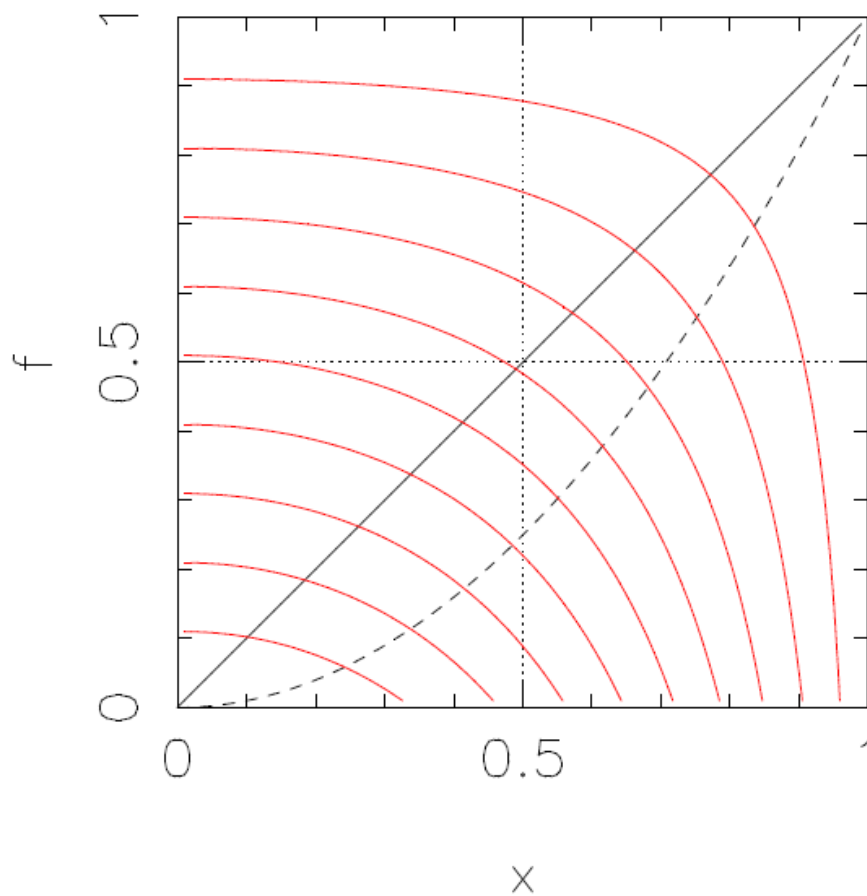


Figure 23 - In the f - x plane the Strehl Ratio contours S are seen to increase from values of 0 to 1 in steps of 0.1 as both f and x ratios increase towards 1. Overlaid are the three considered relationships; $f = x$ (solid), $f = x^2$ (dashed) and $f = 0$ (dot-dash, value 0).

Further investigation shows that these three defined relationships between f and x are also useful when plotting them with increasing Strehl Ratio against increasing core to width ratio x , see figure 24.

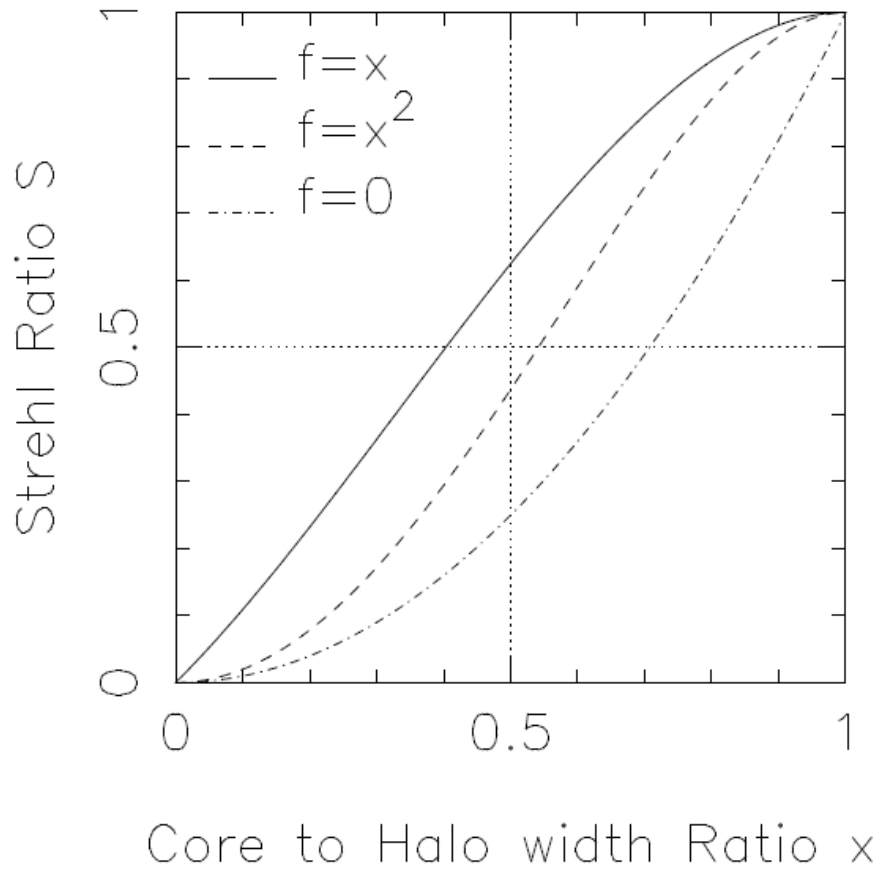


Figure 24 - Strehl Ratio S as a function of core to halo width ratio x as demonstrated for three considered relationships of $f = 0$, x and x^2 , with the greatest improvement in Strehl Ratio occurring for the regime of $f = x$, as can be verified by the plot of improvement factor ϵ versus core to halo width x , see figure 22 above.

The greatest Strehl Ratio is seen to occur for the $f = x$ relationship, that is the upper limit which is in agreement with the plot of improvement factor ϵ versus core to halo width ratio x , see figure 22 above, which had the greatest improvement factor.

3.3.2 Considering a *Moffat* PSF

Though Gaussians are often the most popular choice of PSF shape, the Moffat function^[39] may be adopted as an alternative in cases where the wings (of the halo) may not be accurately portrayed by Gaussian functions. The Moffat has general form

$$P_{mof}(r) = P_{mof0} \frac{1}{\left[1 + \left(\frac{r}{a}\right)^B\right]} \quad (31)$$

Where P_{mof0} is the normalisation factor at peak intensity and r is the radial distance from the peak (i.e. the star's central position $r=0$). The parameter B depends on the power-law exponent in the spectrum of the atmospheric turbulence and determines the overall PSF shape, whilst the parameter a is a scale factor, essentially giving the seeing-limited halo size. For our purposes, the parameter B is adopted from *Baldwin et al*^[40] at a value of $B = 5/3$ which is appropriate for Kolmagorov turbulence, *see section 3.3.3 for further discussion*.

The normalisation factor P_{mof0} was found by integrating the Moffat function for a radial PSF area of $(2\pi r)dr$, giving the general result

$$P_{mof0} = \frac{(B-1)}{\pi a^2} \quad (32)$$

The Moffat may be adopted to fit a more realistic PSF shape due to the broader diminishing of the wings as compared to a Gaussian, *see figure 25* for a visualisation where both functions are plotted for having assumed equal peak intensities, i.e. when $P_{mof0} = P_{gau0}$

Moffat & Gaussian General profiles

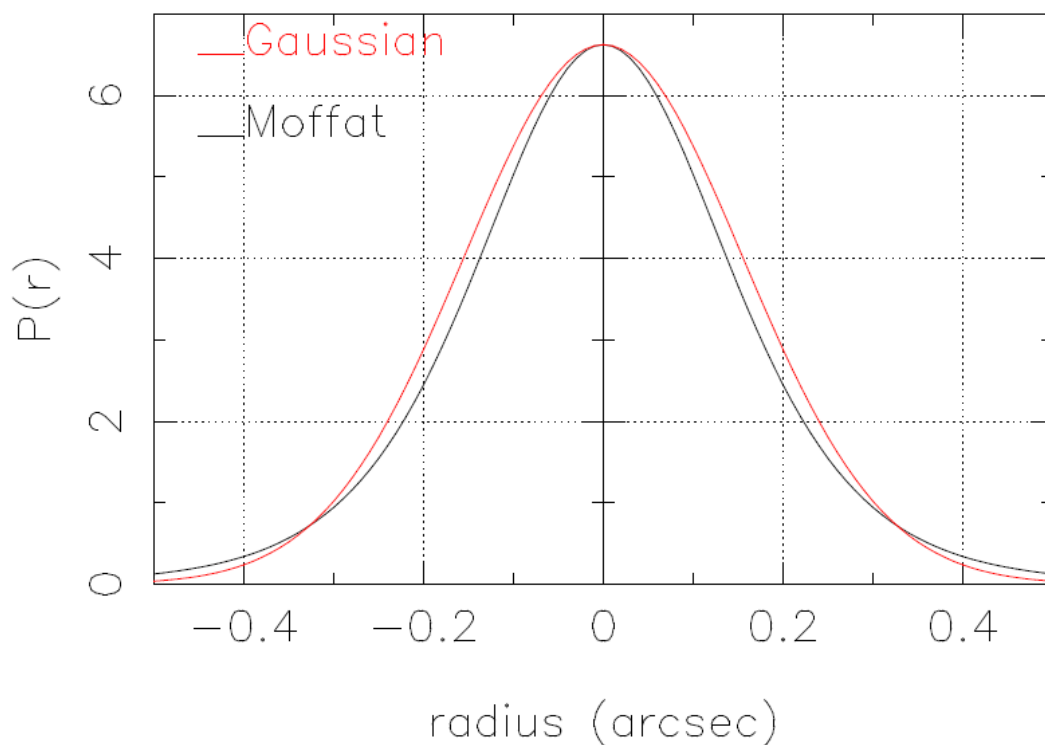


Figure 25 - A Gaussian (red) and Moffat (black) function are compared by having equal peak intensity for their PSF shape, where the Moffat is shown to diminish more gradually in the 'wings', i.e. the halo

In this regime, the Moffat may be used as the lucky PSF (or part of one), in a similar fashion to the Gaussian, where the seeing parameter a may be adopted separately for the core a_c and for the halo a_h (comparable to the difference in Gaussian standard deviations σ_c and σ_h), and still essentially make up the f -dependant lucky PSF.

For our purposes we consider that a more realistic PSF may in fact have a combination of both PSF types; the broader peak of a Gaussian (i.e. in the core), and the broader wings of a Moffat (i.e. in the halo), that is

$$P_L(r) = f \cdot P_{C(Gau)}(r) + (1 - f) \cdot P_{H(Mof)}(r) \quad (33)$$

This raises the question of how to fairly equate two radically different distributions in the same regime. As well as their peak intensity, the two functions may also be compared and equated by their $FWHM$, and by their PSF^2 , where the Moffat seeing parameter $a_{c,h}$ for the core or halo may now be related through the Gaussian's seeing parameter $\sigma_{c,h}$

$$\text{Peaks:} \quad a_{c,h} = \sigma_{c,h} \sqrt{2(B-1)} \quad (34)$$

$$\text{FWHM:} \quad a_{c,h} = \frac{FWHM_{c,h}}{2\sqrt{2^{1/B}-1}} \quad (35)$$

$$\text{PSF}^2: \quad a_{c,h} = \sigma_{c,h} \sqrt{\frac{4(B-1)^2}{2B-1}} \quad (36)$$

For the purposes of this study, the equivalence of the two functions' PSF^2 was used. For fullness of comparison, the use of the Moffat function was examined in three main scenarios with respect to the standard imaging PSF of strictly Gaussian shape:

- 1) As previously outlined, a lucky PSF with a Gaussian Core and a Gaussian Halo (a "*Lucky Gaussian*")
- 2) A lucky PSF with a Moffat Core and a Moffat Halo (a "*Lucky Moffat*")
- 3) Our scenario of interest outlined above; A lucky PSF with a Gaussian Core and a Moffat Halo (a "*Lucky MofGau*")

A sensible visualisation is to examine the PSF profiles of each scenario, with varied fraction f of photons in the core, *see figure 26*.

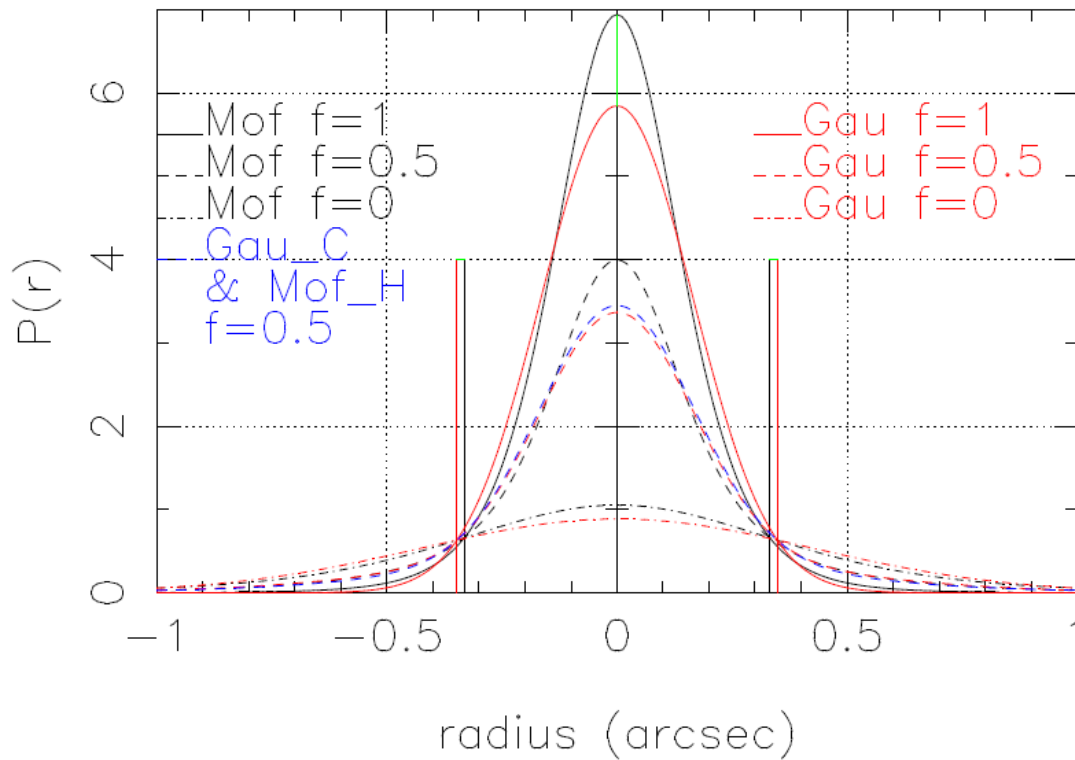
(PSF²) Moffat & Gaussian PSF profiles

Figure 26 - Three regimes are plotted for comparison of the profiles of the PSFs with varied fraction f of photons in the core: **Red** - The original lucky Gaussians, **Black** - the newly generated lucky Moffats, **Blue** - The lucky MofGau, with 50/50 photon contribution to the Moffat halo and the Gaussian core. The boundary markers of core to halo indicate that the Gaussian transition occurs further out from the peak intensity than that of the Moffat transition. Note therefore that logically in the case of the lucky MofGau, its $f = 1$ regime will be exactly equal to the Gaussian $f = 1$, and the $f = 0$ MofGau regime will be exactly equal to the Moffat $f = 0$

Note that as with the lucky Gaussian PSF profiles, the theoretical boundary point r_b of Moffat distributions from core to halo (with varied f) is given in terms of the seeing parameter a by

$$r_b = \pm \sqrt{\frac{\left[\left(\frac{a_H^2}{a_C^2} \right)^{1/B} (a_C a_H)^2 \right] - (a_C a_H)^2}{a_H^2 - a_C^2 \left(\frac{a_H^2}{a_C^2} \right)^{1/B}}} \quad (37)$$

These three scenarios may now be numerically compared through the same analysis applied to the lucky Gaussians in the case of a S/N versus magnitude plot, see figure 27.

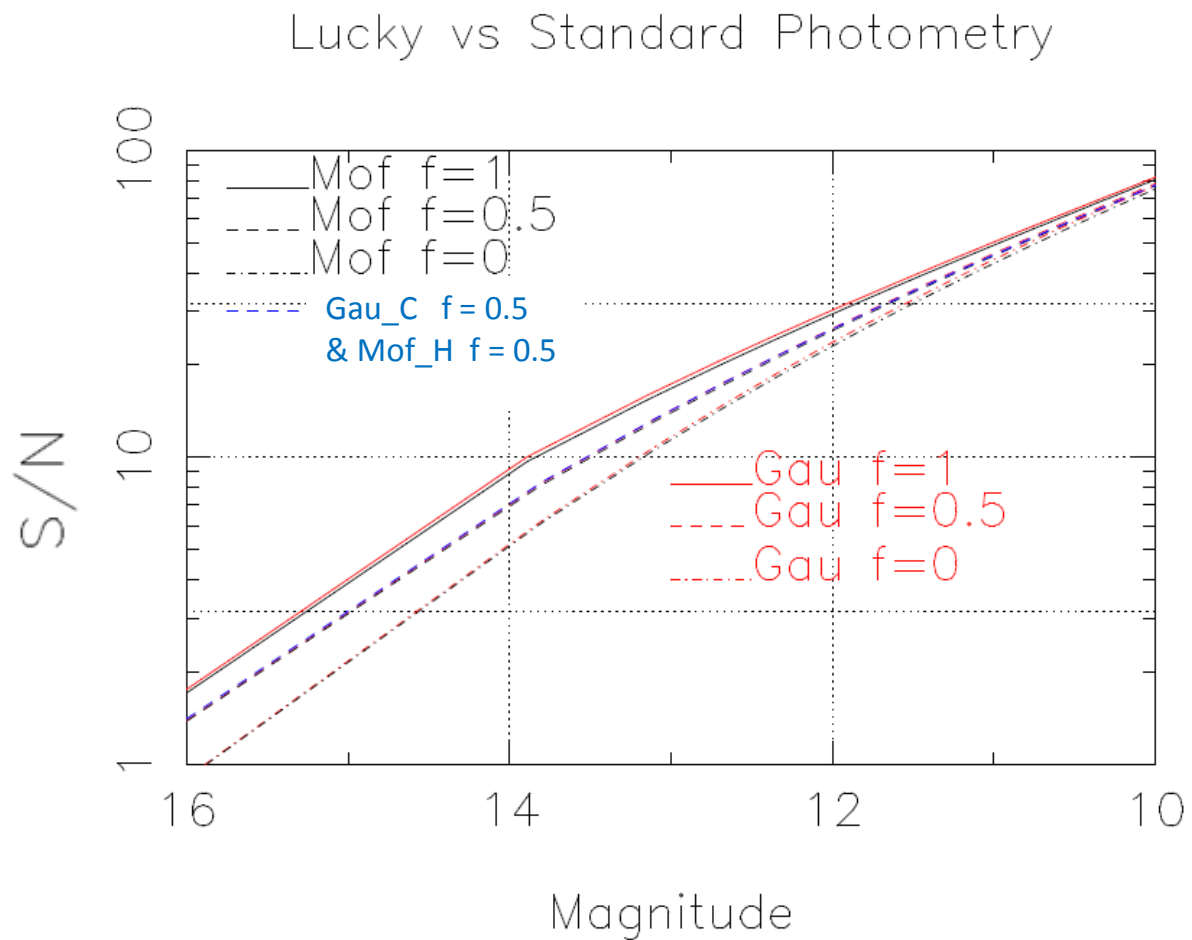


Figure 27 - Three regimes are plotted for comparison with varied fraction f of photons in the core: *Red* - The original lucky Gaussians, *Black* - the newly generated lucky Moffats, *Blue* - The lucky MofGau, with 50/50 photon contribution to the Moffat halo and the Gaussian core. Note therefore that in the lucky MofGau regime, the greatest S/N will be exactly equal to the Gaussian $f = 1$, and the poorest S/N will be exactly equal to the Moffat $f = 0$

For a greater detailed comparison, a further plot was then drawn, normalising each regime to that of the standard-imaging (Gaussian) PSF (which happens to be equal to the Lucky Gaussian regime with $f = 0$), see *figure 28*.

Lucky vs Standard Photometry

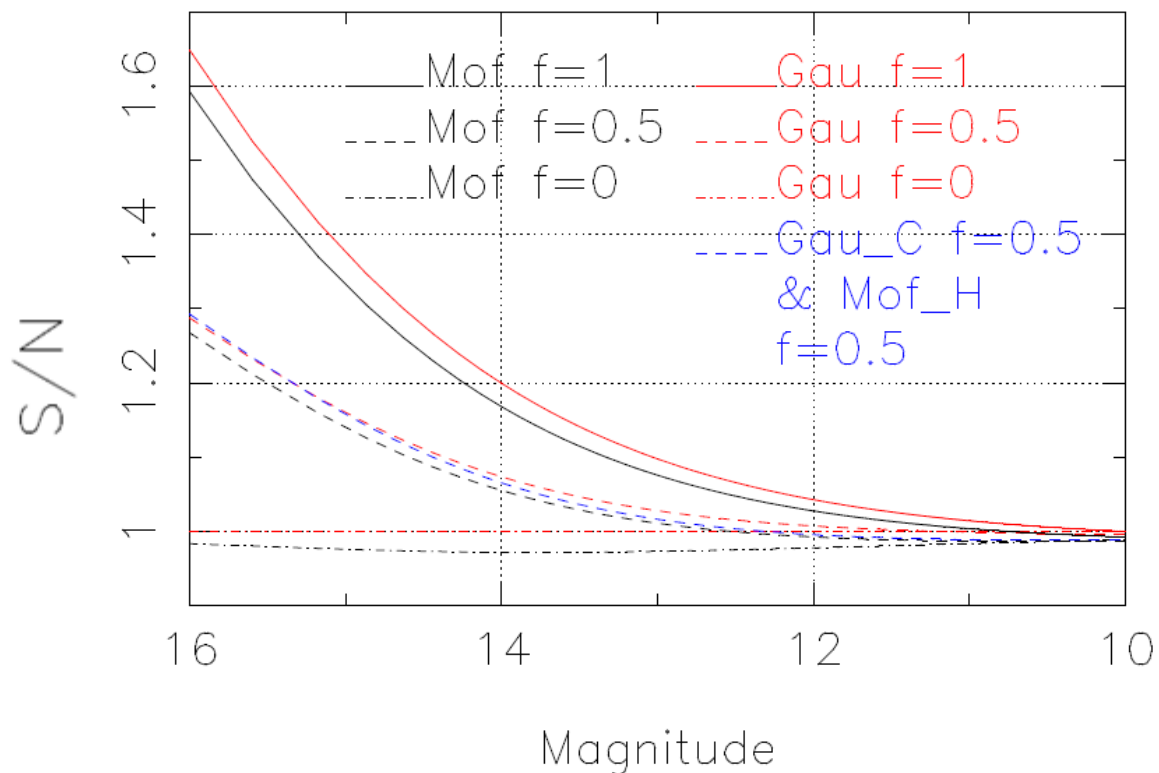


Figure 28 - Plots of the various S/N regimes above, normalised to that of a standard imaging Gaussian PSF. Note that lucky Moffats (black) generally have lesser S/N improvement than lucky Gaussians (red) regardless of the fraction f of photons in the core (though they are in proportion). However, in the case of the lucky MofGau (blue) for $f = 0.5$, there is slightly greater improvement in the extremely fainter star limits than that of the lucky Gaussians with $f = 0.5$

As can be seen, in the case of the lucky MofGau (blue) for $f = 0.5$, there is a slightly greater improvement in the extremely fainter star limits than that of the lucky Gaussians or Moffats with $f = 0.5$, however the improvement is overtaken by the Gaussian PSF for brighter star limits.

In conclusion, theoretically there does not appear to be a significant improvement in S/N when assuming any variation of Moffat (namely MofGau) shape for lucky imaging PSFs; they appear to give poorer or fairly equivalent improvements in comparison with that which is found with Gaussian cores and Gaussian halos - between 25% and 60% improvement in S/N over standard imaging, compared with an 11% improvement for a boxcar model. As the foundations of the theoretical study are now in place for future use and step by step alteration for various factors, any PSF shape may now be tested against the theoretical lucky Gaussian. An investigation which is running in parallel at this institution will determine which of the above PSF shapes are more realistic based on genuine lucky images which are being analysed.

3.3.3 Simulating Seeing-Limited Exposures

In order to gain a theoretical basis from which to analyse exposures taken through the Earth's atmosphere, a simulation was designed which could generate synthetic images and build an understanding of the range of quality seen from seeing-limited through to diffraction-limited photometry.

The objective of the simulation is to provide synthetic images which may themselves have the potential to be analysed for their resultant PSFs, and thus gain insight into the nature of the realistic lucky core/halo shape, and therefore also the most likely relationship between the parameters f and x outlined above. In addition, this will also allow the potential for an investigation into the improvement gained for combinations of varied image stack percentages (e.g. 1% through to 10%) of the highest quality synthetic images sorted by Strehl Ratio, and thus determine the optimum stack combination percentage.

This simulation involves monochromatic light of wavelength λ incident upon a telescope 'pupil plane', producing a resultant image on the 'image plane', before then taking into account the noise and speckles generated by turbulence in the atmosphere. A monochromatic diffraction-limited PSF is the square of the Fourier Transform of the complex amplitude of the light arriving at the pupil of the telescope, where each point on the pupil has a complex number with an amplitude A and a phase ϕ , where the square of the amplitude is the light intensity at that point. The phase varies across the pupil due to the light ray passing through turbulence in the atmosphere, where the variations in index of refraction cause the light to arrive at the pupil with a time delay resulting in speckled images, as discussed in *section 3.3.1*, above.

In order to gain insight into the 2-dimensional simulation required to represent the pixel grid of a pupil plane and image plane, a preliminary investigation into a 1-dimensional case was carried out, thus providing a basis of the computational analysis which would later be required; not unlike first considering the lucky PSF as a boxcar model, before expanding to a more realistic 2-Dimensional Gaussian model.

Firstly a complex rectangular function was set up, with both real and imaginary parts. The surface of the rectangle was given an initial value of 1 representing the telescope pupil, whilst the space outside the rectangle was given an initial value of 0, *see figure 29*.

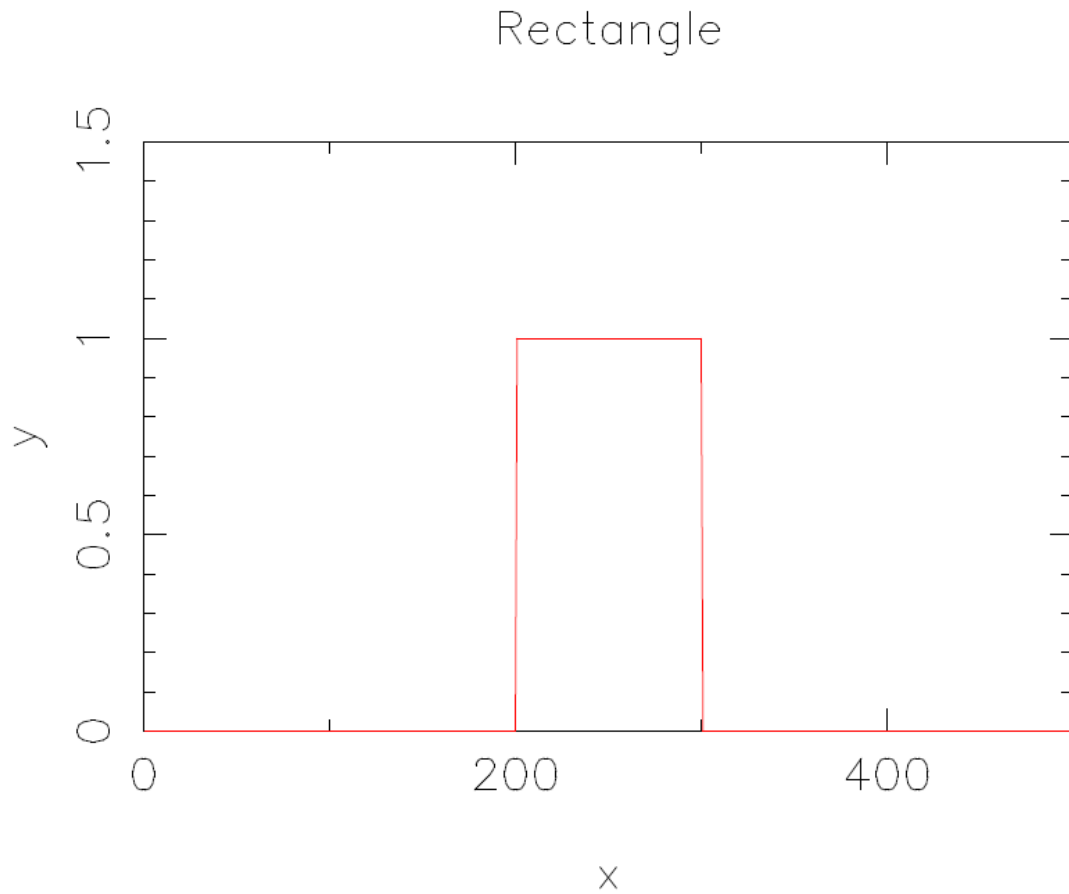


Figure 29 - A complex rectangle function of height 1 on a 1-dimensional grid of 'pixels' represents a simplified aperture surface of a telescope made up of a complex plane.

A Fourier Transform of the function was carried out as an integration over the rectangular function, which according to theory should give rise to the well known *sinc* function^[41], where

$$\int_{-\infty}^{\infty} \text{rect}(t) \cdot e^{-i2\pi ft} dt = \frac{\sin(\pi f)}{\pi f} = \text{sinc}(f) \quad (38)$$

The results of carrying out the equivalent Discrete Fourier Transform over the 1-dimensional rectangular *pupil* grid may be seen in the corresponding 1-dimensional *image* plane, see *figure 30*.

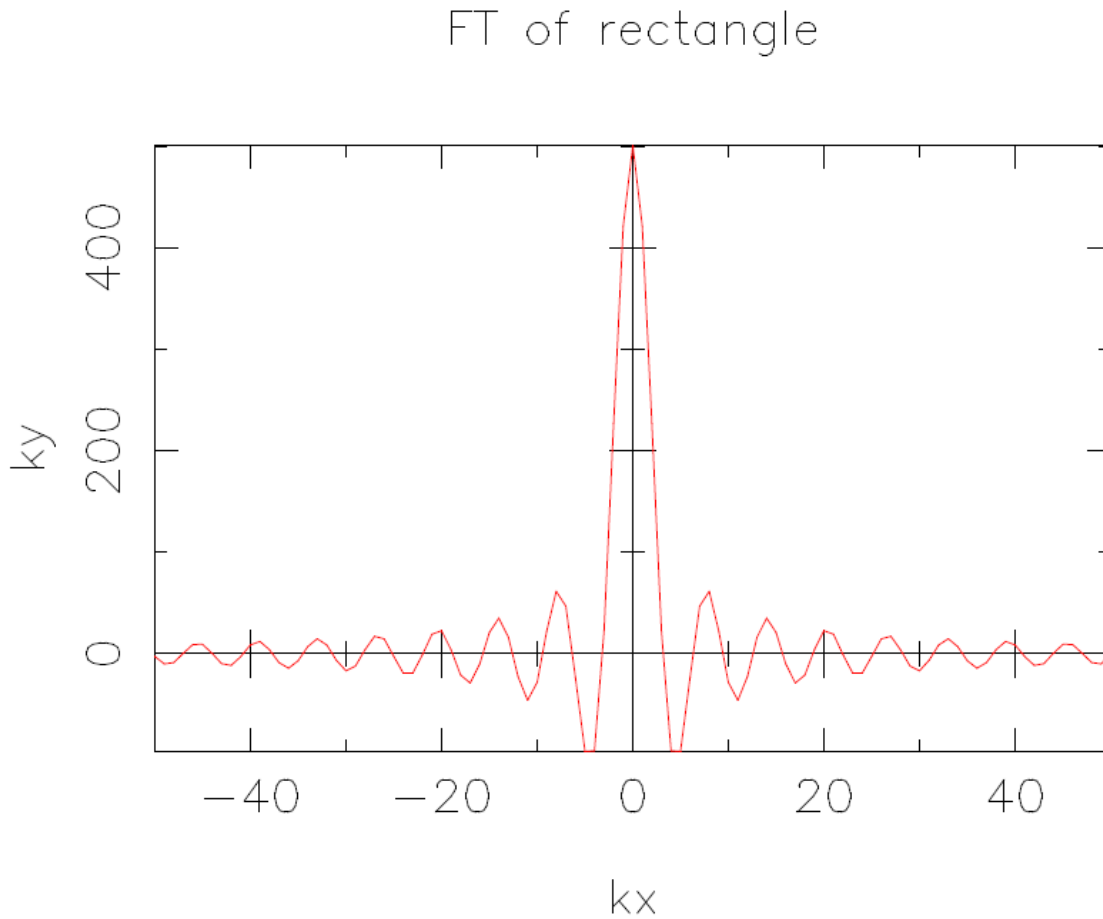


Figure 30 - The DFT (Discrete Fourier Transform) of the rectangular function in figure 22 above produced the *sinc* function (as expected from theory) on the image plane, and for visualisation can be imagined as a central intensity from a star PSF and outlying diminished intensities, much like a halo.

As is expected mathematically, the Fourier Transform of a rectangle function produces the *sinc* function, and is the first test in whether the simulation is functioning correctly prior to being scaled up to a 2-dimensional version.

In order to achieve the 2-dimensional version, firstly a complex circular synthetic telescope pupil was simulated in terms of a grid of pixels $P(x,y)$, with a diameter D twice that of the radius as specified from the central pixel, see figure 31. The area inside the pupil is the active area of interest, and thus was given an initial value of $A_{real} = 1$, whilst the remainder was given value $A_{real} = 0$, with imaginary parts set at default 0, such that the complex pupil plane may be expressed by

$$P(x, y) = A_{real} + iA_{imaginary} \quad (39)$$

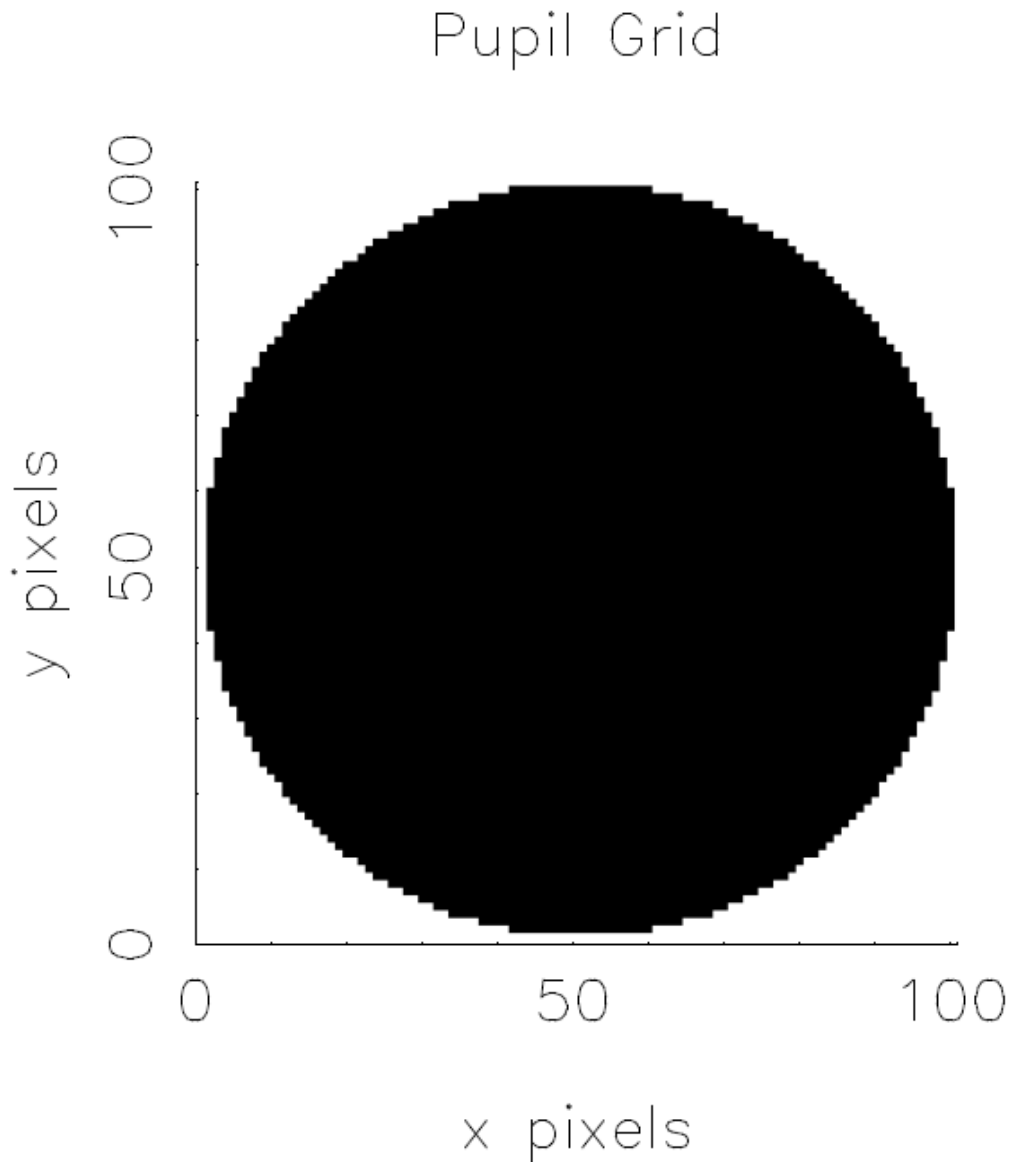


Figure 31 - The original complex 2-dimensional simulation of a telescope Pupil set up as a grid $P(x,y)$ of pixels. The circular pupil is given an initial 'intensity' value of 1 to represent the light incoming from a distant star (black), whilst the remainder is set to 0 (ie where light is not gathered by the pupil, white).

A Fourier Transform was then carried out over the entire pupil grid $A(x,y)$ similarly to that of the rectangular function, to produce the resultant image on the new corresponding image plane with brightness $B(k_x, k_y)$ such that in general,

$$B(k_x, k_y) = \int P(x, y) \cdot e^{-i(k_x \cdot x + k_y \cdot y)} \quad (40)$$

The image plane was then plotted similarly in an image pixel grid, *see figure 32*, where highlighted profile slices were taken at several intervals from the radius in order to investigate the nature of the resultant function.

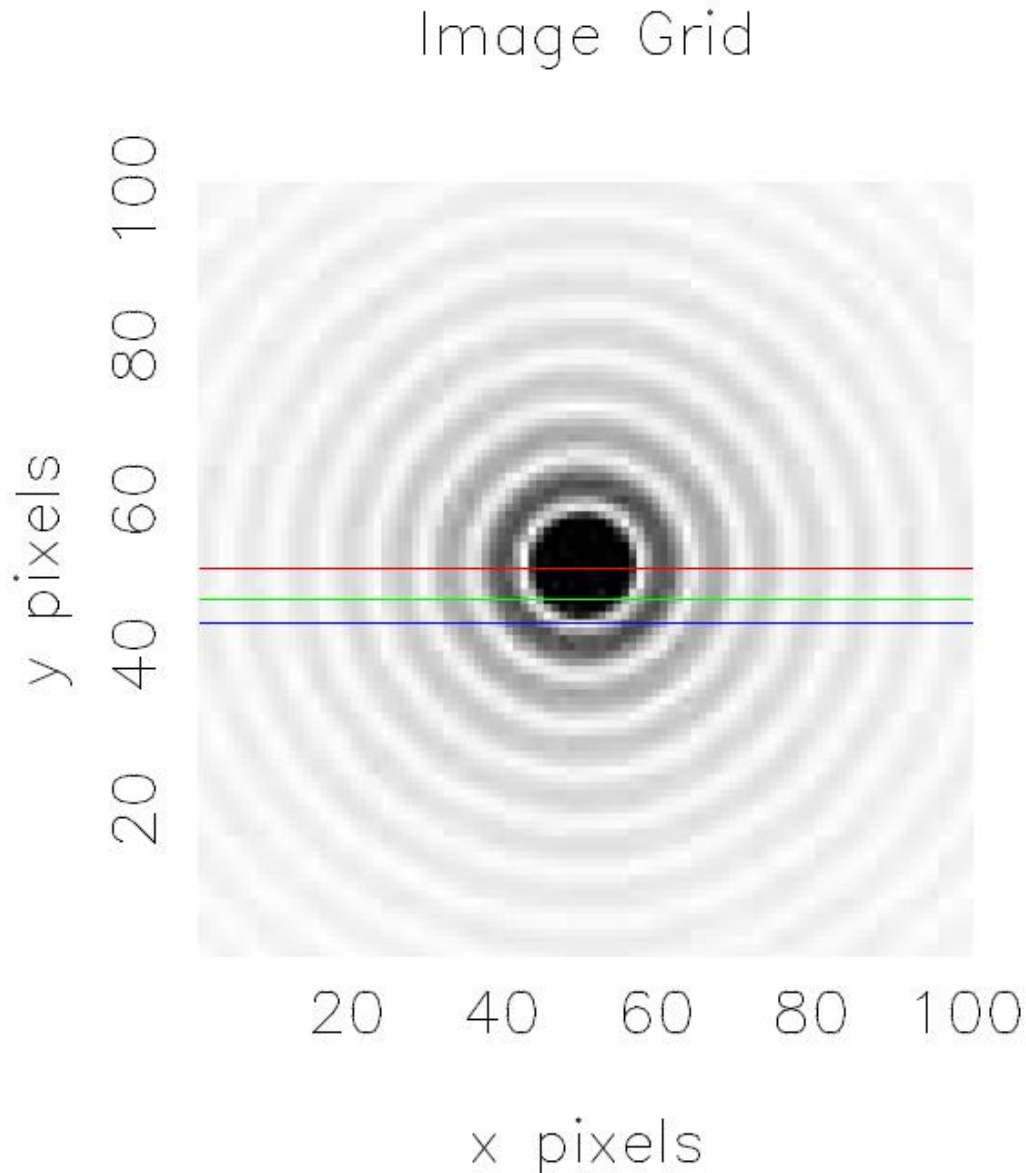


Figure 32 - The Fourier Transform from the circular aperture results in an Airy Function with a bright centre and airy rings of diminishing intensity. Three profiles slices are highlighted from the centre in order to investigate the function, see figure 33. Note, the greyscale colours of the PSF have been inverted and enhanced in order to emphasise the repeating Airy pattern.

As demonstrated, for monochromatic light of wavelength λ incident on a circular pupil of diameter D , the 'perfect' PSF is an Airy function with a width λ/D shown as rings of diminishing intensity from the central peak. The profile slices at the highlighted positions were then plotted for confirmation into the varying intensity, see figure 33, indicating that as with the 1-dimensional case, the simulation is indeed functioning correctly, and ready to be developed further given sound theoretical foundations. Note that the profile slices from the 2D Fourier Transform are mathematically equivalent to the square of the sinc function produced by the 1D Fourier Transform.

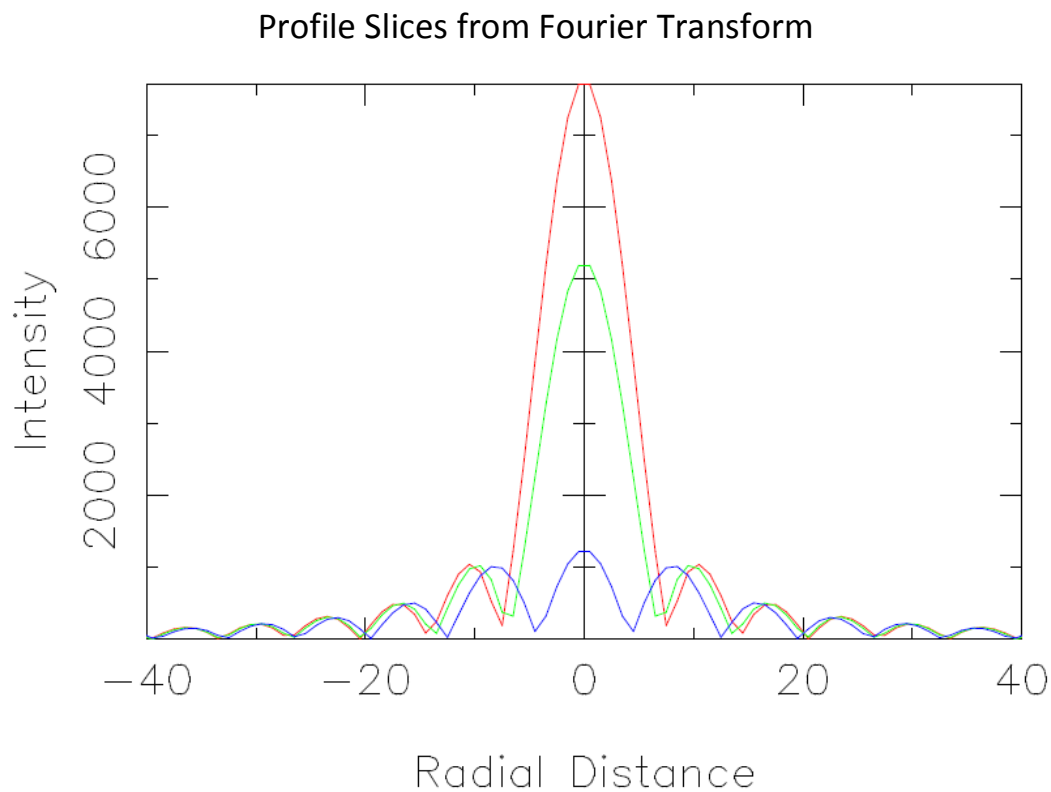


Figure 33 - The 1-dimensional Profile slices of the Fourier Transform reveal that the radial intensities diminish as expected in a typical Airy Pattern, with a peak intensity at the centre, and is theoretically comparable to the square of the sinc function generated from the DFT of the rectangular function.

Given that the aim of the simulation is to recreate a realistic image as seen by a true telescope, another addition to the process is to consider another limitation of a typical reflecting telescope - that is the effect of the secondary mirror, *see figure 34*, on the resultant PSF.

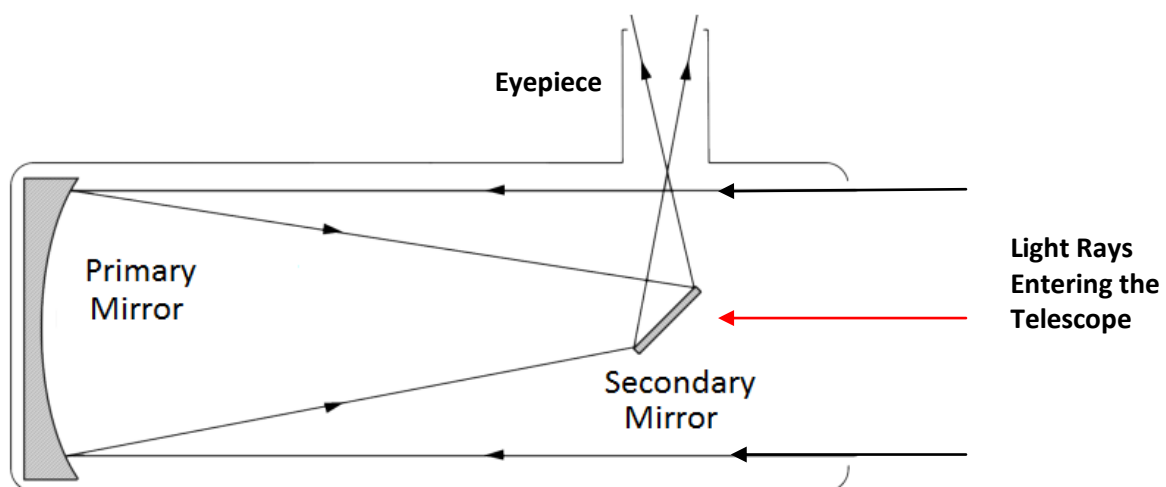


Figure 34 - Diagram of a typical Newtonian Reflecting Telescope, where a secondary mirror redirects the light into the eyepiece, however it also serves as an obscuration as it blocks the initial incoming light in its path, leading to deviations in the resultant image. Diagram adapted from LCOGT.net^[42]

In order to simulate this effect, an exaggerated (for illustrative purposes) circular obscuration representing the secondary mirror was placed in the pupil grid prior to the Fourier Transform to result in the new image. A further implementation was to include physical 'supports' for the mirror in the form of thin beams representing typical wires which hold the mirror in place, once again greatly exaggerated for demonstrative effect of the resultant PSF. See figures 35 - 37.

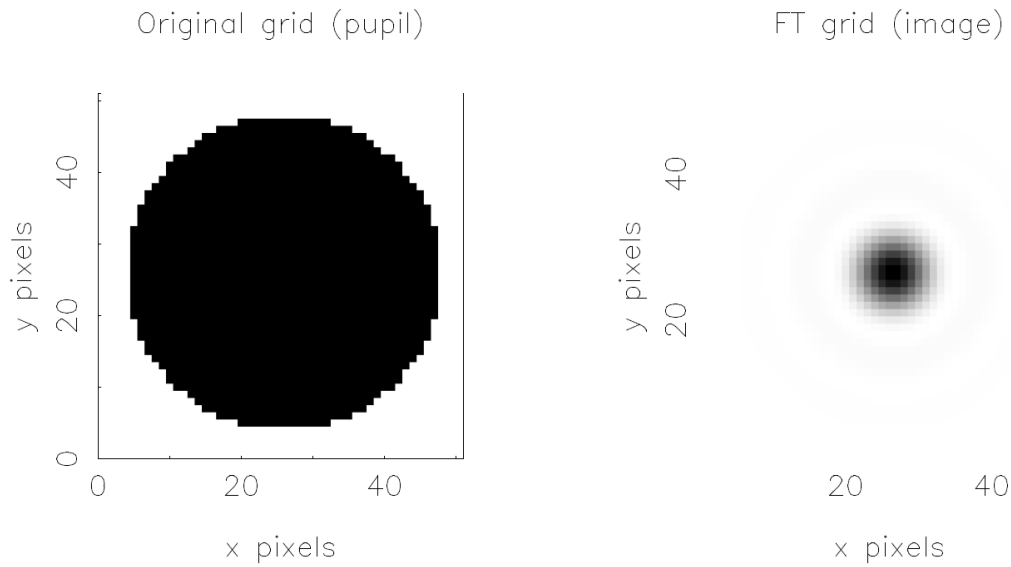


Figure 35 - Left, the original Pupil grid is Fourier Transformed to result in the PSF on the image grid, right, which is a centrally intense Airy Disk (this greyscale has not been altered).

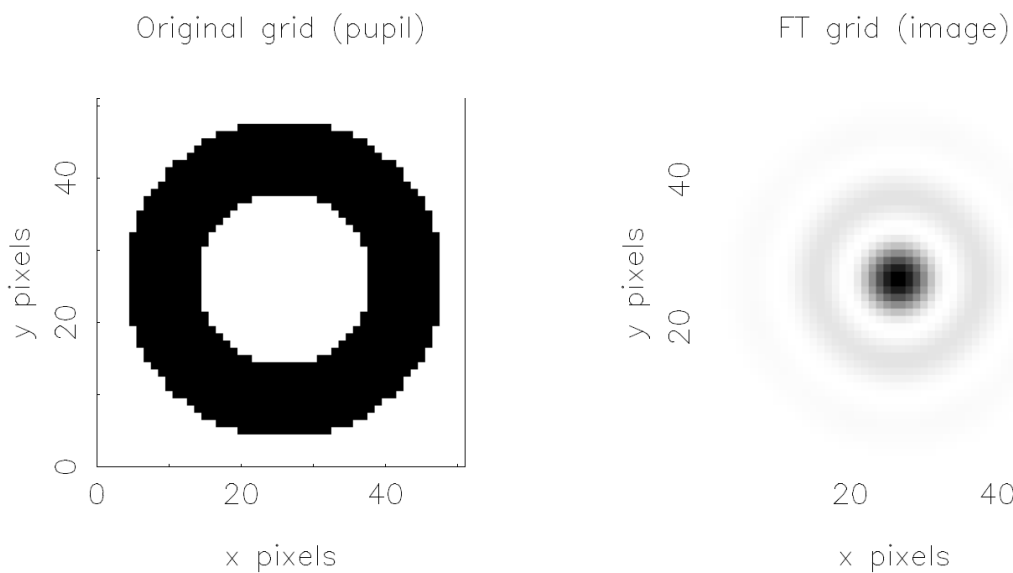


Figure 36 - Left, an exaggerated obscuration representing the secondary reflecting mirror of the telescope is placed in the pupil plane, whose Fourier Transform results in the more pronounced Airy Pattern, right, with a notable ring shape outside of the central intensity.

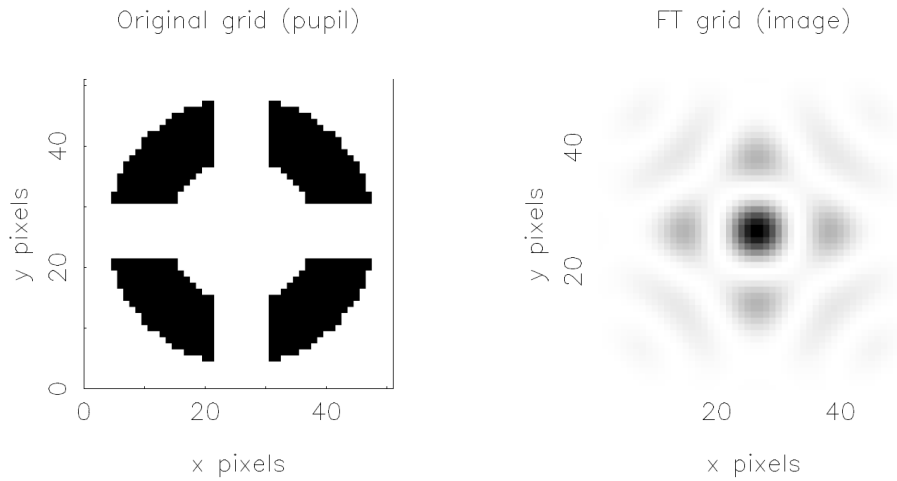


Figure 37 - Left, in addition to the secondary mirror, further obscurations representing the mirror's physical supports are added, the result of which is a further disrupted PSF, **right**, due to the square shape of the supports.

In addition to the obscuration, a single-case linear phase ramp was introduced across the pupil, which occurs because the time-dependent change of arrival position for speckles will cause a shift in the pattern, and thus the offset is the first basic approximation for a one-time atmospheric shift. That is to say the star is not statically at the same position, but rather changes its effective position with respect to the pupil, due to seeing factors.

For the complex amplitude A of the pupil plane, the Fourier Transform to the image plane with brightness B has a phase ϕ such that

$$A(x, y) = B(x, y) \exp(i\phi(x, y))$$

Where the linear phase ramp may be written as the dot product of the wavevector k in the pupil plane and the position vector x in the pupil plane

$$\phi(x, y) = kx \cdot x + ky \cdot y$$

The PSF will then shift in the image plane (without further distortion) proportionally to the wavevector k , see figure 38.

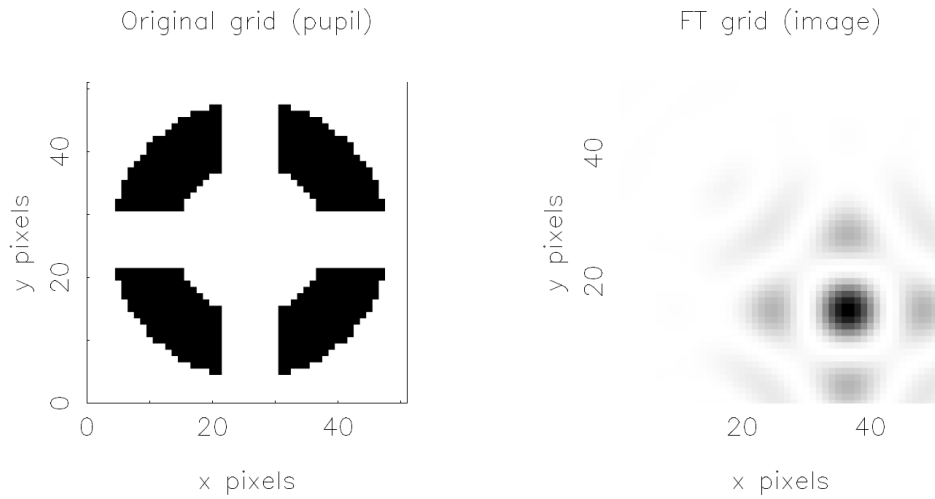


Figure 38 - Including a phase ramp in the simulation results in a shift in the PSF's position without affecting the overall shape, owing to the time-dependant change of the arrival position for the speckles.

Given the inherently random nature of atmospheric turbulence, the next step of the simulation is to scale up the above effect and randomise the phase ramp (leading to a random position of the PSF), as well as to include the speckling effect that results in the constant changes of refractive index throughout the atmosphere. Following the reconstruction of the obscuration of the secondary mirror to a more realistic (smaller) one, this is achieved by applying a further 2-dimensional grid to the Fourier Transform from the pupil plane of *randomised Gaussian numbers*.

The brightness level B of the image may now be given by the Fourier Transform of the pupil P with respect to some amplitude A and some phase ϕ

$$B(\vec{x}) = P(\vec{x})(1 + A(\vec{x}))\exp(i\phi(\vec{x}))$$

Where the phase is given by

$$\phi(\vec{x}) = \sum_k \phi_{\vec{k}}(\vec{x})$$

And where

$$\phi_{\vec{k}}(\vec{x}) = C_{\vec{k}} \cos(\vec{k} \cdot \vec{x}) + S_{\vec{k}} \sin(\vec{k} \cdot \vec{x})$$

Where C and S represent the 2D Random Gaussian grids required for the phase component, with mean $\mu = 0$ and variance σ^2 , giving

$$C_{\vec{k}} = \text{Gaussian}(0, \sigma_k^2), \quad S_{\vec{k}} = \text{Gaussian}(0, \sigma_k^2)$$

And similarly, the Amplitude A may now be defined as

$$A(\vec{x}) = \sum_k A_{\vec{k}}(\vec{x})$$

Where

$$A_{\vec{k}}(\vec{x}) = CA_{\vec{k}} \cos(\vec{k} \cdot \vec{x}) + SA_{\vec{k}} \sin(\vec{k} \cdot \vec{x})$$

And where CA and SA represent the 2D Random Gaussian grids required for the Amplitude component, also with mean $\mu = 0$ and variance σ^2 , giving

$$CA_{\vec{k}} = \text{Gaussian}(0, \sigma_k^2), \quad SA_{\vec{k}} = \text{Gaussian}(0, \sigma_k^2)$$

These random numbers govern a random change to the intensity of each pixel, resulting in distortion of the entire image, the extent of which is dependent on the standard deviation in the Gaussian distribution - that is, the spread and extent of the speckling will increase with increasing standard deviation, *see figure 39*.

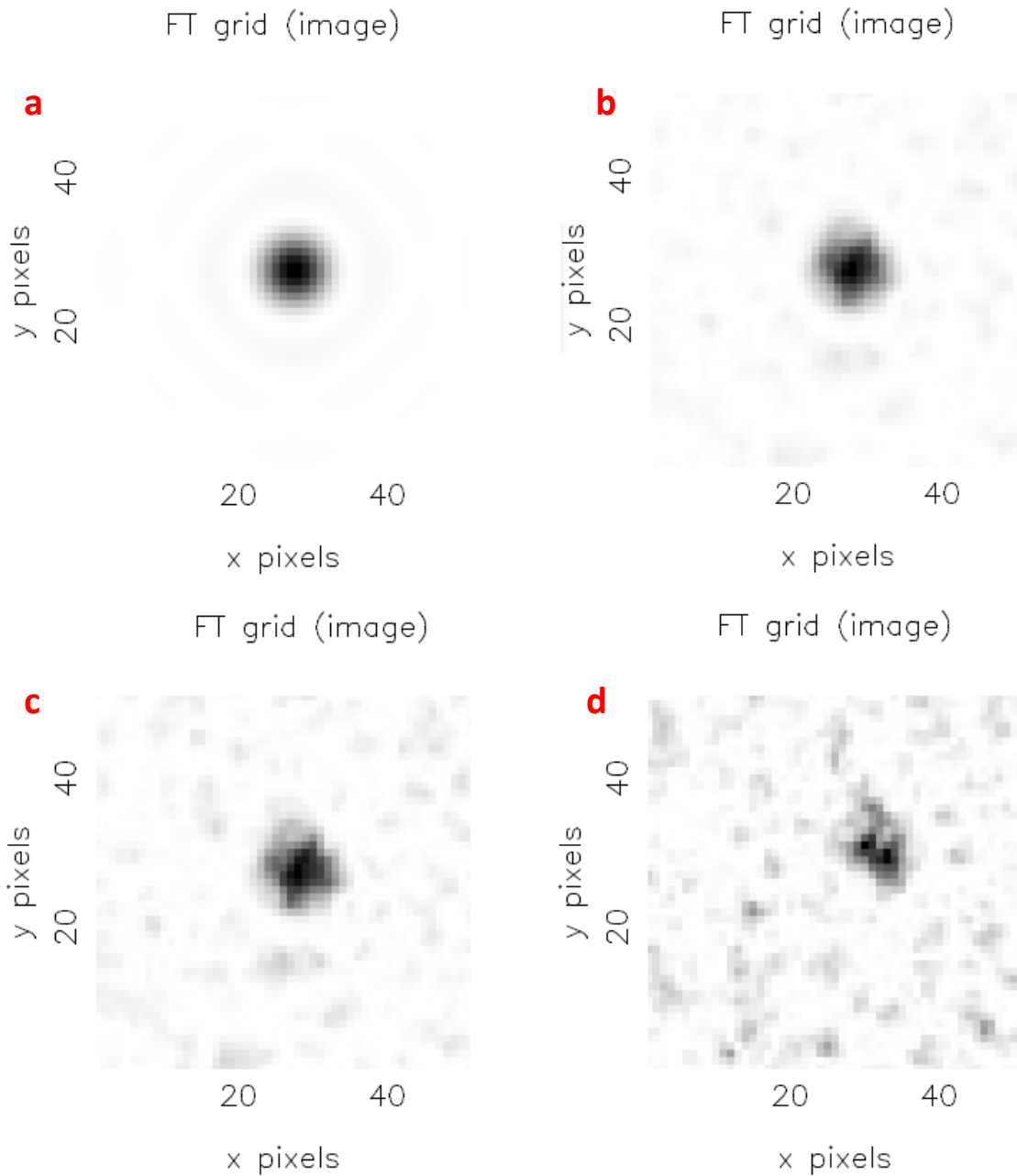


Figure 39 - From *a* to *d*: Demonstrating the effects on the resulting image plane of increasing the standard deviation of the Gaussian Random Numbers which represent the atmospheric changes; increasing the standard deviation (spread) of the numbers increases the randomised changes in intensity, and results in increased speckling of the image.

Note therefore that the image of *figure 39a* represents that which would be expected with no randomised atmospheric turbulence at all, i.e. when the standard deviation in the random Gaussian numbers is 0, or equivalent to purely diffraction-limited photometry.

The most realistic standard deviation σ (or variance, σ^2) of the Gaussian distribution is adapted from the work on the so-called *Kolmogorov Model* which was developed by Tatarski^[44] based on the initial investigations on turbulence by Kolmogorov^[43]. The model includes the power exponent $5/3$ which is determined as the typical value for the Kolmogorov model of typical atmospheric conditions^[35] *as discussed in section 3.3.2 above*.

$$\sigma^2 = 1.0299 \left(\frac{D}{r_0} \right)^{5/3} \quad (41)$$

Where r_0 is the *Fried Seeing Parameter*^[44], which is a measure of the optical quality of the atmosphere given in centimetres. This is to correspond directly with the aperture diameter D of the telescope, and thus gives a measure of the extent of turbulence and whether this will be comparable with seeing-limited or diffraction-limited observations; typical values of the Fried parameter are *10cm* for average seeing (as used in this simulation) and *20-40cm* for very good seeing conditions.

An approximate lucky imaging technique may now be adopted whereby for each image, the random turbulence changes slightly, representing the sub-second exposure time typical of each lucky image. The next step after taking several exposures is to stack them on the brightest pixel, where increasing the number of original exposures in the stack will gradually converge on an image which could potentially appear to have not been affected by atmospheric turbulence, *see figures 40 and 41*.

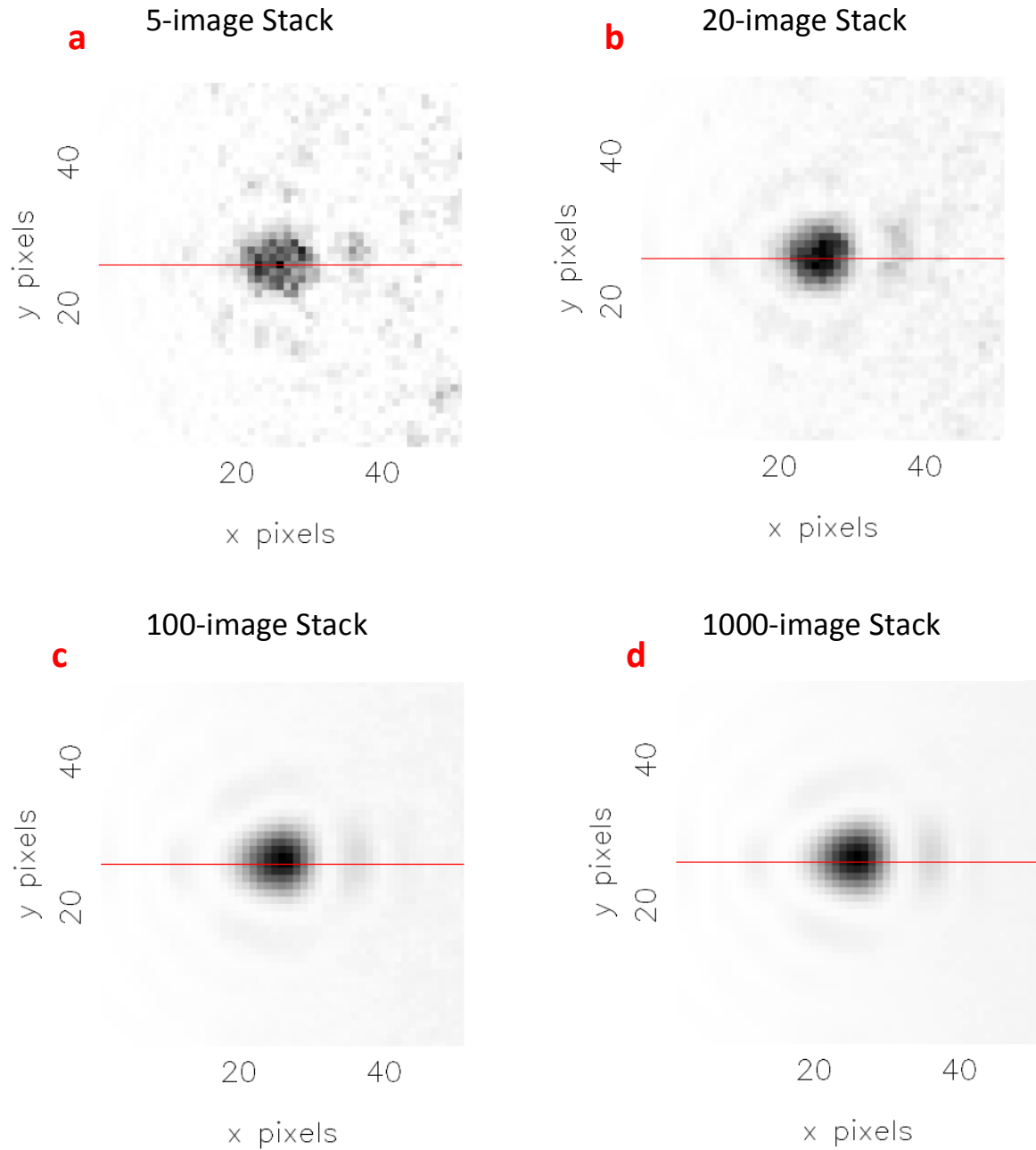


Figure 40 - From a to d: The effects of increasing the number of exposures (5, 20, 100 and 1000 respectively) which are stacked to produce the resultant images. The new PSFs are visibly smoother, and the speckling effect has been reduced as a result of stacking the randomised raised and lowered intensities of the turbulence effects. This has effectively reconstructed an approximation to the 'true' PSF which may be expected in diffraction-limited photometry (i.e. photometry from space) and is comparable to the original image produced in *figure 39a* before adding the turbulence effects. The red lines represent the profile slice taken for use in *figure 41*.

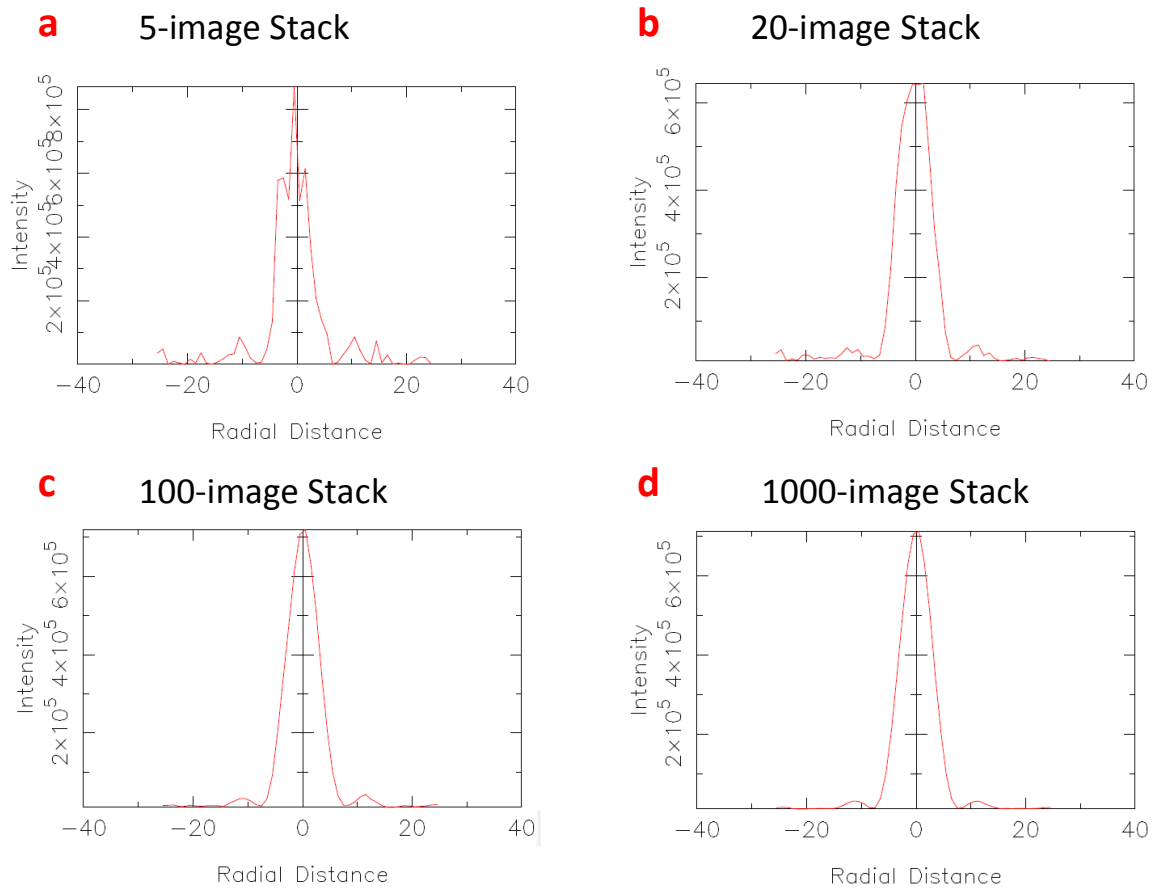


Figure 41 - From a to d: The profile slices of the respective simulated images produced in *figure 40* illustrate that an increase in exposures used in the stack converge on a reasonable approximation to that of a diffraction-limited image, such as that seen in the airy profile in *figure 33*.

The results clearly indicate that very short exposures which are stacked in this way can reduce the effects of atmospheric turbulence, and with an increase of stacked images converge on an approximation of diffraction-limited photometry. As a result, the simulation is now primed to accept and process the Fourier Transform from any type of pupil plane to an image plane, with customisable seeing conditions (i.e. ranging from very good to very poor seeing), as well as stacking a custom number of exposures to lead to the final lucky image.

3.3.4 Limitations & Future Expansion of the Simulation

Whilst the basis of the simulation is operational and the functions are customisable, a number of improvements should be considered for its future use.

Firstly, as outlined in the theory above, the stacking process of lucky images does not typically involve *all* exposures produced, only the highest 1-10% quality, where the quality is selected based on the Strehl Ratio, which may be measured based on the resultant point-spread functions.

Secondly, a mathematical analysis of the simulated lucky images should be carried out, whereby simulated 2-dimensional lucky PSFs *outlined in section 3.3.2* may be constructed and compared with the simulated lucky exposures. This would involve developing pixel grids of 2-dimensional PSFs with various core and halo distributions, such as Gaussian, Moffat or as studied, the *Lucky MofGau* with a Moffat halo and a Gaussian core.

An MCMC algorithm may compare the simulated lucky images for example by a Chi-Squared fit, and answer definitively which type of core/halo arrangement is realistic. Finally, using real lucky images, the same analysis may be carried out, and further compared with the synthetic lucky images in order to have both a practical and theoretical basis of the potential improvements of lucky imaging.

4.0 Conclusions

Whilst constantly developing upon the modelling techniques used for gravitational microlensing events is vital, so too is selecting the highest quality subset of the available data (magnification images) for reduction before being used in the modelling process.

Subsequently, even more important is the gathering of the raw data itself. There is huge potential in adapting the lucky imaging technique in microlensing photometry in order to ensure the best models are fit to the best selection of quality data, and thus analyse more precisely the characteristics of detected extrasolar planets. The mathematical results indicate a significant improvement in lucky imaging Signal to Noise Ratio over standard imaging, and is therefore worth further continued analysis and exploration in order to determine precisely the realistic improvement.

This is further confirmed by an early-stage simulation of the lucky imaging process, which has illustrated that stacking sub-second lucky exposures is capable of reducing the speckling effect which occurs due to atmospheric turbulence, essentially producing images which are indeed potentially comparable to diffraction-limited photometry.

In conclusion, a quantitative investigation into increasing the quality of the original photometric data available from any gravitational microlensing event demonstrates that 'lucky imaging' can lead to a marked improvement in the signal to noise ratio over that of standard imaging techniques. The improvement to the original images obtained by lucky imaging, together with critical sub-selection of images in the reductions process, leading to improved simulations and model-fitting has the potential of resulting in more accurate analysis, and thus may lead to the calculation of more accurate planetary parameters, as well as the detection and confirmation of otherwise more difficult planetary candidates.

5.0 Future Work

5.1 Constraints on Microlensed Systems using Lucky Imaging

Several important constraints may be placed on a microlensed system such as the planet and star mass, by high resolution imaging several years *after* the event in order to detect the star flux, colour and proper motion. There is immense interest in continuing some themes outlined above, including testing the lucky imaging technique on appropriate events, where an astrometric colour shift may be seen after several years. This could then extend to looking at all planets discovered so far and making the relevant calculations when revisiting them; given that lens and source stars come from different populations and different masses, they inherently have different colours, and so taking images of the microlensing events several years later with lucky imaging using two filters, one may expect to see the change in position and investigate important constraints for the system which could begin with estimates from the FTS/FTN lucky imagers in the very near future. Lucky imaging would be essential here given the precise and delicate nature of the calculations required for astrometry, where lucky imaging gives the best chance of high quality photometry with minimal atmospheric interference.

5.2 Observing

One highly anticipated and beneficial aspect of undertaking a project in microlensing is the invitation to take part in observing runs during each season. Particularly interesting and unique events such as planetary candidates often feature in typical astronomy theses, and dependant on their rarity may lead to further, more intensive investigations. I was invited to complete the following workloads:

- 2 weeks observing with the Danish 1.54m telescope^[45] at La Silla, Chile

The Danish telescope is operated in person on site, the first week of which is spent under the training of an experienced observer, and the following week is spent training the next observer on site.

- 1 week remote observing with MONET 1.2m telescope^[46] at SAAO, South Africa

The MONET telescope is operated remotely in a semi-automatic manner, which requires a remote observer to start up, monitor the semi-automatic microlensing observations fed to the telescope via ARTEMiS^[47], obtain calibrations, and shut down the telescope following an observing night.

In addition to the practical knowledge and understanding gained through such intense astronomical observing at La Silla and SAAO, the work itself also allows membership of the MiNDSTeP Consortium^[48] for that year. Members are entitled to co-author papers which result from the observations collected during that period, where typically one year of membership will give rise to co-authorship of 5 or more peer-reviewed scientific papers.

6.0 Publications

This section contains summarised information regarding any publications, having been submitted or currently in draft, on which I have co-authorship and which have been completed in connection with Gravitational Microlensing during this Project. Many aspects of the computational or mathematical theory outlined in this thesis are often used to complete scientific papers such as these, with many groups around the world collaborating and sharing data and expertise in order to contribute towards various sections within.

"Microlensing Binaries with Brown Dwarf Companions" (*Submitted August 2012*); I. -G. Shin, C. Han, A. Gould and others including D. Bajek^[49]

An investigation of microlensing events which have been identified as binary systems containing brown dwarf companions; objects with masses between that of large gas giant planets and low-mass stars. Of seven candidate events selected for analysis, two have been confirmed to contain such brown dwarfs.

"MOA-2010-BLG-073Lb: A Cool, Low Mass Brown Dwarf Orbiting an M-Dwarf" (*Accepted by ApJ November 2012*); R.A. Street, J.-Y Choi, Y. Tsapras, C. Han and others including D. Bajek

This paper also discusses an event which includes a brown dwarf, but was of particular interest as the source star of the event had previously been known to be photometrically variable, however the investigation indicates that the source is actually an *irregular* variable and is a red giant.

"A Cool Jupiter-Mass Planet in Microlensing Beyond the Snow Line in Event OGLE-2011-BLG-0251" (*Submitted to A&A, October 2012*); N. Kains, R. Street, C. Han, A. Udalski and others including D. Bajek

This paper discusses the discovery of a Jupiter-mass planet in a microlensing event, and outlines the techniques used to determine its characteristics, and establish the separation from its host star, which is beyond the snow line. Given the rarity of planets discovered by the microlensing technique, publications of all occurrences are vital in drawing collaborations to assist in the complex nature of their analysis.

"Photometric Potential of Lucky Imaging"; (*In Draft*), K. Horne, D. Bajek, K. Harpsoe

As outlined in section 3.0, a theoretical investigation into the benefit of lucky imaging photometry over standard imaging photometry. This includes the potential numerical improvement in the signal to noise under various circumstances, and the results of a simulation demonstrating the lucky imaging technique.

7.0 References

- [1] Wolszczan, A., Frail, D. (1992). "A planetary system around the millisecond pulsar PSR1257 + 12". *Nature* 355 (6356): 145–147.
- [2] Schneider, Jean "Interactive Extra-solar Planets Catalog". The Extrasolar Planets Encyclopedia
- [3] http://en.wikipedia.org/wiki/Extrasolar_planet
- [4] G. Chauvin; A.M. Lagrange; C. Dumas; B. Zuckerman; D. Mouillet; I. Song; J.-L. Beuzit; P. Lowrance (2004). "A giant planet candidate near a young brown dwarf". *Astronomy & Astrophysics* 425 (2): L29 – L32
- [5] D.J. Erskine, J. Edelstein, D. Harbeck and J. Lloyd (2005). "Externally Dispersed Interferometry for Planetary Studies". In Daniel R. Coulter. *Proceedings of SPIE: Techniques and Instrumentation for Detection of Exoplanets II*. 5905. pp. 249–2
- [6] Hidas, M. G.; Ashley, M. C. B.; Webb, et al. (2005). "The University of New South Wales Extrasolar Planet Search: methods and first results from a field centred on NGC 6633". *Monthly Notices of the Royal Astronomical Society* 360 (2): 703–717
- [7] Benedict et al.; McArthur, B. E.; Forveille, T.; Delfosse, X.; Nelan, E.; Butler, R. P.; Spiesman, W.; Marcy, G. et al. (2002). "A Mass for the Extrasolar Planet Gliese 876b Determined from Hubble Space Telescope Fine Guidance Sensor 3 Astrometry and High-Precision Radial Velocities". *The Astrophysical Journal Letters* 581 (2): L115–L118
- [8] http://www.esa.int/SPECIALS/Operations/SEMK5HZTIVE_0.html
- [9] Einstein, Albert (1936). "Lens-like Action of a Star by the Deviation of Light in the Gravitational Field". *Science* 84 (2188): 506–507
- [10] Alcock, C. et al. (1993). "Possible gravitational microlensing of a star in the Large Magellanic Cloud". *Nature* 365 (6447): 621–623
- [11] <http://wfirst.gsfc.nasa.gov/about>
- [12] Gould, A., 2000 "A Natural Formalism for Microlensing". *The Astrophysical Journal* 542
- [13] Horne, K. et al (2009) "A metric and optimization scheme for microlens planet searches" *Monthly Notices of the Royal Astronomical Society*, Vol. 396, No. 4., pp. 2087–2102
- [14] Paczyński, Bohdan (1996) "Gravitational microlensing in the Local Group", *Annual Review of Astronomy and Astrophysics*, 34: 419
- [15] Di Stefano, R. (2005) "Mesolensing Explorations of Nearby Masses: From Planets to Black Holes", *The Astrophysical Journal*, V684, Issue 1: 59-67.
- [16] Di Stefano, R. (2009) "New opportunities in microlensing and mesolensing" *The Astronomy and Astrophysics Decadal Survey*, Science White Papers, no. 65
- [17] Di Stefano, R., & Night, C. (2008) "Discovery and Study of Nearby Habitable Planets with Mesolensing" *Harvard-Smithsonian Center for Astrophysics*.
- [18] Lepine, S. & Di Stefano, R. (2012) "On the detectability of a predicted mesolensing even associated with the high proper motion star VB 10" *ApJ* 749 L6

- [19] Di Stefano, R. et al (2012) "Searching for Planets During Predicted Mesolensing Events: Theory, and the Case of VB 10" arXiv:1202.5314v1
- [20] http://en.wikipedia.org/wiki/Rogue_planet
- [21] Sumi, T., Kamiya, K., Bennett, D. P., et al. (2011) "Unbound or distant planetary mass population detected by Gravitational Microlensing" 2011, *Nature*, 473, 349
- [22] Quanz, S. P. et al (2012) "Direct imaging constraints on planet populations detected by microlensing" arXiv:1203.3647v1
- [23] Veras, D., & Raymond, S. N. (2012), "Planet-planet scattering alone cannot explain the free-floating planet population" arXiv:1201.2175
- [24] Stevenson, D.J. (1998) "Possibility of Life-sustaining Planets in Interstellar Space" *Nature* 400, 32
- [25] Lissauer, J.J., (1987) "Timescales for Planetary Accretion and the Structure of the Proto-planetary disk" *Icarus* 69: 249–265
- [26] Abbot, D.S. & Switzer, E.R (2011) "The Steppenwolf: A proposal for a habitable planet in interstellar space" arXiv:1102.1108v2
- [27] Baross, J. A., and Hoffman, S. E. 1985, *Origin of Life*, 15, 327
- [28] Debes, J.H & Sigurdson, S. (2007) "The Survival Rate of Ejected Terrestrial Planets with Moons" arXiv:0709.0945v1
- [29] John Archibald Wheeler, "The 'Past' and the 'Delayed-Choice' Double-Slit Experiment", in *Mathematical Foundations of Quantum Theory*, edited by A.R. Marlow, p. 13
- [30] <http://www.space.com/529-quantum-astronomy-double-slit-experiment.html>
- [31] Jacques, Vincent; et al. (2007). "Experimental Realization of Wheeler's Delayed-Choice Gedanken Experiment". *Science* 315: 966–968
- [32] Dominik, M., et al. 2007, *MNRAS*, 380, 792
- [33] <http://ogle.astrouw.edu.pl/ogle4/ews/2011/ews.html>
- [34] TATARSKI, V. I. (1961). "Wave Propagation in a Turbulent Medium", McGraw-Hill Books
- [35] Tubbs, R. N., (2003) "Lucky Exposures: Diffraction limited astronomical imaging through the atmosphere", Cambridge University
- [36] Fried, D. (1978). "Probability of getting a lucky short-exposure image through turbulence". *Optical Society of America* 68 (12): 1651–1658
- [37] Fried, D. (1966). "Optical Resolution Through a Randomly Inhomogeneous Medium for Very Long and Very Short Exposures". *Optical Society of America Journal* 56 (10): 1372
- [38] Strehl, K. (1895), "Aplanatische und fehlerhafte Abbildung im Fernrohr", *Zeitschrift für Instrumentenkunde*, 362-370
- [39] Moffat, A.F.J. (1969) "A Theoretical Investigation of Focal Stellar Images in the Photographic Emulsion and Application to Photographic Photometry" *Astronomy and Astrophysics*, Vol. 3, p. 455 (1969)
- [40] Baldwin, J.E. (2008) "The point spread function in Lucky Imaging and variations in seeing on short timescales" *A&A* 480, p589–597

- [41] Woodward, P. M.; Davies, I. L. (1952). "Information theory and inverse probability in telecommunication". *Proceedings of the IEE - Part III: Radio and Communication Engineering* 99 (58): 37–44
- [42] <http://lcogt.net/spacebook/reflecting-telescopes>
- [43] Kolmogorov, A. N. (1941) "The local structure of turbulence in incompressible viscous fluid for very large Reynolds numbers". *Proceedings of the USSR Academy of Sciences* 30: 299–303
- [44] Fried, D. L. (1966). "Optical Resolution Through a Randomly Inhomogeneous Medium for Very Long and Very Short Exposures". *Journal of the Optical Society of America* 56 (10): 1372–1379
- [45] <http://www.eso.org/public/teles-instr/lasilla/danish154.html>
- [46] <http://monet.uni-goettingen.de/foswiki>
- [47] <http://www.artemis-uk.org/>
- [48] <http://www.mindstep-science.org/>
- [49] "Microlensing Binaries with Brown Dwarf Companions" (2012); I. -G. Shin, C. Han, A. Gould et al, arXiv:1208.2323v1
- [50] G. Chauvin, A.-M. Lagrange, C. Dumas, B. Zuckerman, D. Mouillet, I. Song, J.-L. Beuzit, P. Lowrance (2004) "A giant planet candidate near a young brown dwarf" *Direct VLT/NACO observations using IR wavefront sensing, Astronomy and Astrophysics* 425, pp. L29–L32
- [51] D. Bennett, I. Bond et al (2004), "The Microlensing Planet Finder: Completing the Census of Extrasolar Planets in the Milky Way", *Proceedings of the SPIE Astronomical Telescopes and Instrumentation Symposium*
- [52] D. Bennet, J. Anderson et al (2010) "Completing the Census of Exoplanets with Microlensing Planet Finder (MPF)", arXiv:1012.4486v1
- [53] <http://www.iau.org>
- [54] Y. Tsapras, R. Street, K. Horne et al (2009), "RoboNet-II: Follow-up observations of microlensing events with a robotic network of telescopes" *Astronomische Nachrichten*, Vol.330, Issue 1, p.4
- [55] C. Snodgrass, Y. Tsapras, R. Street et al (2008), "The web-PLOP observation prioritisation system", *PoS(GMC8)056*
- [56] D. M. Bramich (2008), "A New Algorithm for Difference Image Analysis", arXiv:0802.1273v1
- [57] Bond, I. A. et al. (2004). "OGLE 2003-BLG-235/MOA 2003-BLG-53: A Planetary Microlensing Event". *The Astrophysical Journal Letters* 606 (2): L155–L158. arXiv:astro-ph/0404309